

1  
2  
3  
4 Direct measurement of critical resolved shear stress of prismatic  
5 and basal slip in polycrystalline Ti using high energy X-ray  
6  
7 diffraction microscopy  
8  
9  
10  
11  
12  
13  
14

15 L. Wang<sup>1,2\*</sup>, Z. Zheng<sup>1</sup>, H. Phukan<sup>2</sup>, P. Kenesei<sup>3</sup>, J.-S. Park<sup>3</sup>, J. Lind<sup>4,5</sup>, R.M.  
16 Suter<sup>4</sup>, T.R. Bieler<sup>2</sup>  
17  
18

19 <sup>1</sup> School of Materials Science and Engineering, Shanghai Jiao Tong University,  
20 China  
21  
22

23 <sup>2</sup> Department of Chemical Engineering and Materials Science, Michigan State  
24 University, USA  
25  
26

27 <sup>3</sup> Advanced Photon Source, Argonne National Laboratory, USA  
28  
29

30 <sup>4</sup> Department of Physics, Carnegie Mellon University, USA  
31  
32

33 <sup>5</sup> Lawrence Livermore National Laboratory, USA  
34  
35  
36

37 \*Corresponding author  
38  
39 Email: [leyunwang@sjtu.edu.cn](mailto:leyunwang@sjtu.edu.cn) or [wly857@gmail.com](mailto:wly857@gmail.com)  
40  
41

42 Phone: +86 21-54740838  
43  
44

45 Postal Address:  
46  
47

48 School of Materials Science and Engineering  
49 Shanghai Jiao Tong University  
50 800 Dongchuan Road, Shanghai 200240, China  
51  
52  
53  
54  
55  
56  
57  
58  
59  
60  
61  
62  
63  
64  
65

1  
2  
3  
4  
**Abstract**  
5  
6

7 Knowledge of the critical resolved shear stress (CRSS) values of different slip modes is  
8 important for accurately modeling plastic deformation of hexagonal materials. Here, we  
9 demonstrate that CRSS can be directly measured with an in-situ high energy X-ray diffraction  
10 microscopy (HEDM) experiment. A commercially pure Ti tensile specimen was deformed up to  
11 2.6% strain. In-situ far-field HEDM experiments were carried out to track the evolution of  
12 crystallographic orientations, centers of masses, and stress states of 1153 grains in a material  
13 volume of  $1.1\text{mm}\times 1\text{mm}\times 1\text{mm}$ . Predominant prismatic slip was identified in 18 grains, where the  
14 orientation change occurred primarily by rotation around the c-axis during specimen deformation.  
15 By analyzing the resolved shear stress on individual slip systems, the estimated CRSS for  
16 prismatic slip is  $96\pm 18$  MPa. Predominant basal slip was identified in 22 other grains, where the  
17 orientation change occurred primarily by tilting the c-axis about an axis in the basal plane. The  
18 estimated CRSS for basal slip is  $127\pm 33$  MPa. The ratio of  $\text{CRSS}_{\text{basal}}/\text{CRSS}_{\text{prismatic}}$  is in the range  
19 of 1.7–2.1. From indirect assessment, the CRSS for pyramidal  $\langle c+a \rangle$  slip is likely greater than  
20 240 MPa. Grain size and free surface effects on the CRSS value in different grains are also  
21 examined.

22  
23  
24  
25  
26  
27  
28  
**Keywords**  
29  
30

31 Critical resolved shear stress; Titanium; Crystal plasticity; High-energy X-ray diffraction; In situ  
32 tension test  
33  
34  
35  
36  
37  
38  
39  
40  
41  
42  
43  
44  
45  
46  
47  
48  
49  
50  
51  
52  
53  
54  
55  
56  
57  
58  
59  
60  
61  
62  
63  
64  
65

1  
2  
3  
4  
5  
6  
7 **1. Introduction**

8  
9 Titanium and its alloys are widely used in aerospace and biomedical industries. For  
10 manufacturers, material strength under complicated loading conditions is a key consideration for  
11 product design. At the grain scale, material yielding corresponds to the activation of slip systems  
12 in individual grains. Critical resolved shear stress (CRSS) for different slip modes is therefore  
13 important information for material design. As a hexagonal material, Ti has four major slip modes;  
14 namely,  $\{0001\} < \bar{1}\bar{2}10 >$  basal slip,  $\{10\bar{1}0\} < \bar{1}\bar{2}10 >$  prismatic slip,  $\{10\bar{1}1\} < \bar{1}\bar{2}10 >$  pyramidal  
15  $<\text{a}>$  slip, and  $\{10\bar{1}1\} < 2\bar{1}\bar{1}\bar{3} >$  pyramidal  $<\text{c+a}>$  slip [1, 2]. Among them, prismatic slip is the  
16 easiest mode to be activated [3–5]. It is difficult to assess the CRSS of individual slip modes by  
17 deforming a large single crystalline material though, as multiple slip and twinning activities can  
18 occur simultaneously during deformation and thus complicate the analysis. As a result, CRSS of  
19 individual slip modes in Ti are more often determined by three alternative methods.  
20  
21  
22  
23  
24  
25  
26  
27  
28  
29  
30  
31  
32  
33  
34  
35  
36  
37

38 The first method is to statistically count the observations of slip lines from different slip modes in  
39 a deformed polycrystalline aggregate. Grain orientations are measured by electron backscattered  
40 diffraction (EBSD) or transmission electron microscopy (TEM) in order to identify the activated  
41 slip systems by trace analysis and to estimate their Schmid factors based upon a global stress.  
42 Applying certain statistical assumptions, the relative CRSS ratios between different slip modes  
43 can be identified. Table 1 shows the obtained CRSS ratios in the literature, determined by slip  
44 line trace analysis [6–8]. This method, however, usually does not provide the absolute CRSS  
45 values unless in-grain slip activity can be monitored from an in-situ test inside a scanning  
46 electron microscope (SEM) [8]. As the stress state in each grain is not necessarily equal to the  
47 macroscopic applied stress [9], this introduces variability into the conditions in which slip occurs.  
48  
49  
50  
51  
52  
53  
54  
55  
56  
57  
58  
59  
60  
61  
62  
63  
64  
65

The second method is based on crystal plasticity modeling. A polycrystalline specimen with measured initial texture is deformed by a mechanical test, and the deformation process is simulated using a crystal plasticity model. By comparing the stress-strain curves, texture evolution, and deformation details within individual grains between experimental observation and model prediction, an optimal set of CRSS values for different slip modes can be ~~obtained~~inferred.

Table 1 shows the CRSS values of different slip modes in Ti reported in the literature, determined by crystal plasticity modeling [10–17]. Most of the models include  $\{10\bar{1}2\} < \bar{1}011 >$  (T1 twinning) as an additional deformation mode, whose CRSS values are also shown in Table 1. Significant variation of the CRSS values is evident in the table. Part of the variation can be attributed to the different oxygen concentration and grain size of the materials. However, sometimes even for materials with similar oxygen concentration and grain size, the reported CRSS values can be quite different (e.g. [11] and [15]). This difference reflects intrinsically different constitutive frameworks used in those models, including the number of slip and twin modes that are allowed to be activated.

The third method uses micromechanical testing of small single crystal specimens prepared by focused ion beams (FIB). The advantage of this method is that a crystal orientation favorable for a specific slip mode can be pre-selected and machined for testing, which makes the measurement more controllable. Table 1 shows the measured CRSS of a commercially pure Ti material from microcantilever bending experiments performed by Gong and Wilkinson [18,19]. This method, however, requires an advanced SEM and experienced operators to conduct sample preparation and subsequent micromechanical testing. Effects due to surface damage and the small sample volume also introduce some variability in the data [20].

In this present study, a fourth method to measure CRSS of different slip modes in hexagonal materials is presented. It is based on in-situ mechanical testing of a polycrystalline specimen and the use of far-field high energy X-ray diffraction microscopy (HEDM) to track the deformation history of individual grains. Far-field HEDM, also known as three-dimensional X-ray diffraction (3DXRD), was first developed at Risø National Laboratory in Denmark by Poulsen et al. and implemented at the European Synchrotron Radiation Facility (ESRF) [21–24]. A high energy monochromatic X-ray beam is used to illuminate the entire cross section of a polycrystalline sample. Diffraction peaks from all grains that satisfy the diffraction condition are recorded using an area detector as the sample is rotated with respect to the X-ray beam. These diffraction peaks are then indexed to obtain the crystallographic orientation, centers of mass (COMs), and average stress state of individual grains in the sample volume illuminated by the X-ray [23–29]. When this analysis process is repeated for different deformation steps of while deforming a sample under load (i.e. in situ test), microstructure evolution in individual grains can be characterized. In situ far-field HEDM has been used to investigate the micromechanical behavior of polycrystalline materials such as twin nucleation events in individual grains in polycrystalline Mg, Ti, and Zr alloys [9, 30–34].

In the present work, we use this method is used to analyze selected grains that deformed by a predominant dislocation slip system. In a far-field HEDM experiment the activated slip system(s) in a grain can be analyzed from the shape of its diffraction peaks [35–38]. Using a forward modeling approach: the shape of the diffraction peaks in selected grains are simulated assuming activation of one or more slip systems, then the simulation result is compared with the measured diffraction peaks to identify the most likely slip system(s) that can account for the observation.

1  
2  
3  
4  
5  
6  
7  
8  
9  
10  
11  
12  
13  
14  
15  
16  
17  
18  
19  
20  
21  
22  
23  
24  
25  
26  
27  
28  
29  
30  
31  
32  
33  
34  
35  
36  
37  
38  
39  
40  
41  
42  
43  
44  
45  
46  
47  
48  
49  
50  
51  
52  
53  
54  
55  
56  
57  
58  
59  
60  
61  
62  
63  
64  
65

Here, a different approach is used to identify The activated slip mode can be identified for individual  
the active slip systems in a larger number of grains based on the continuous rotation of  
the grainsgrain orientation by tracking their orientation rotation during deformation. In particular, prismatic slip causes a grain to gradually rotate around its  $<0001>$  axis, while basal slip causes a grain to gradually tilt its  $<0001>$  axis about an axis residing in the basal plane. With knowledge of the average stress state tensor in each grain (which can be significantly different from the global stress state tensor [9, 34]), the resolved shear stress (RSS) on the corresponding activated slip system can be directly calculated and directly identified as athe CRSS value. This analysis is performed for many grains that show predominant prismatic slip or predominant basal slip to obtain average CRSS values for the two slip modes. By comparing the RSS of different slip modes when one slip mode is activated and the others are not, we can also estimate the CRSS ratio between basal slip and prismatic slip. The influence of the grain size and the free surface on the CRSS value in different grains is also studiedexamined. This analysis neglects the expected inhomogeneous stress distributions within grains, which can result incontributes to the variations in apparent CRSS values among different grains.

## 2. Experimental

The in situ far-field HEDM experiment was conducted at the Advanced Photon Source (APS) beamline 1-ID-E as illustrated in Figure 1. A tensile sample of Grade 1 commercially pure Ti, with a cross sectional area of  $1 \times 1 \text{ mm}^2$  and gauge length of 5mm, was mounted in a specially designed load frame [3539]. The chemical composition of the material is shown in Table 2. The material contained nearly equiaxed grains with average grain size of  $\sim 100 \mu\text{m}$ , as determined from previous EBSD analysis [12]. A strong  $\{0001\}$  texture close to the tensile axis was present in the sample. A  $100 \mu\text{m}$  tall by 1.5 mm wide monochromatic X-ray beam (Energy=65.4keV<sub>z</sub>)

1  
2  
3  
4  $\lambda=0.0189\text{nm}$ ) illuminated the entire cross section of the sample as it was rotated with respect to  
5 the X-ray beam. Following the principles of far-field HEDM [23], the sample was rotated about  
6 the tensile axis (Z) over a [-70°, 70°] range and diffraction patterns were recorded on an  
7 amorphous Si area detector placed approximately 1.0 m away from the sample as  $\omega$  swept  
8 through 1° intervals. The sample was deformed incrementally by tension with 30 steps, followed  
9 by 7 steps of unloading. The stress-strain curve, derived from the load-displacement data  
10 assuming uniform macro-scale deformation, is shown in Figure 1. At each deformation step, a  
11 far-field HEDM measurement was performed while the displacement of the load frame crosshead  
12 was held constant during the  $\omega$  scan(i.e. rotating the sample and collecting a diffraction pattern at  
13 each  $\omega$  interval). To establish a large data set for statistical analysis, the measurement was  
14 performed in 11 adjacent layers along the sample gauge. A digital image correlation (DIC)  
15 camera was used to measure macroscopic strain and to ensure that approximately the same  
16 volume was illuminated at all 37 deformation steps, which is critical for tracking individual  
17 grains through the test.

18  
19  
20  
21  
22  
23  
24  
25  
26  
27  
28  
29  
30  
31  
32  
33  
34  
35  
36  
37  
38  
39  
40  
41 Grain indexing from the collected diffraction patterns was implemented using the FABLE  
42 software package jointly developed by ESRF and Risø National Laboratory [23,~~3640~~]. For each  
43 far-field HEDM measurement, diffraction patterns at each  $\omega$  step were processed by the  
44 *PeakSearch* program in FABLE to identify all peaks above a certain intensity threshold. The  
45 *Transformation* program transformed the peak positions from the Cartesian coordinate on the  
46 detector into a 20- $\eta$  diagram. The 20- $\eta$  diagram at the undeformed state was used to determine  
47 the instrument parameters including sample-to-detector distance, detector tilt, and direct beam  
48 position on the detector. With an optimal set of instrument parameters, then converts these  
49 diffraction peaks can be converted into reciprocal lattice vectors (i.e. g-vectors) in the 3D space  
50  
51  
52  
53  
54  
55  
56  
57  
58  
59  
60  
61  
62  
63  
64  
65

1  
2  
3  
4 based on the Ti crystal structure and the calibrated detector information (distance, tilt, beam  
5 center, etc.). Finally, the *GrainSpotter* program was used to index grains and determine their  
6 crystallographic orientations based on these reciprocal lattice vectors. The minimum threshold to  
7 recognize a grain is that at least 40 peaks were assigned to that grain when the macroscopic strain  
8 is less than 0.3%, and at least 30 peaks were assigned to that grain when the macroscopic strain is  
9 above 0.3%. In most of the recognized grains, the number of identified peaks was often far  
10 greater than the threshold value. For example, the average number of identified peaks for the  
11 recognized grains in layer 6 is 56 at load step 1 ( $\varepsilon=0$ ), 54 at load step 9 ( $\varepsilon=0.31\%$ ), and 50 at load  
12 step 29 ( $\varepsilon=2.6\%$ ), as shown in Table 3. An independent Matlab code [31] was additionally used  
13 to obtain COMs and the elastic strain tensor of each indexed grain using ~~at least 30~~the position of  
14 all of the diffraction peaks ~~diffraction spots per grain and through~~ least squares fitting. The  
15 average uncertainty (i.e. error bar) for COM position ( $\Delta X$ ,  $\Delta Y$ ) and elastic strain components  
16 ( $\Delta e_{ij}$ ) can be calculated from the covariance matrix of the estimates for the least squares fit, and  
17 these values are shown in Table 3. ( $\Delta X$ ,  $\Delta Y$ ) is in the range of 20–30  $\mu\text{m}$ , which is less than half  
18 of the average grain size.  $\Delta e_{ij}$  is around  $3 \times 10^{-4}$ . As a rough estimation using the bulk modulus  
19 (110 GPa) and the shear modulus (44 GPa) of Ti, this translates to uncertainty of about 33 MPa for  
20 normal stress components and 12 MPa for shear stress components. At load step 1, the average  
21 magnitude of ( $\Delta e_{XX}$ ,  $\Delta e_{ZZ}$ ,  $\Delta e_{ZX}$ ) is comparable to the average elastic strain components ( $e_{XX}$ ,  $e_{ZZ}$ ,  
22  $e_{ZX}$ ). After the tensile test began, the magnitude of ( $e_{XX}$ ,  $e_{ZZ}$ ,  $e_{ZX}$ ) rapidly increased, diminishing  
23 the impact of ( $\Delta e_{XX}$ ,  $\Delta e_{ZZ}$ ,  $\Delta e_{XY}$ ). At load step 9 ( $\varepsilon=0.31\%$ ), absolute values of  $e_{XX}$  ( $13 \times 10^{-4}$ ) and  
24  $e_{ZZ}$  ( $22 \times 10^{-4}$ ) already became 4 and 7 times of  $\Delta e_{XX}$  and  $\Delta e_{ZZ}$ , respectively. Because this is the  
25 stage when slip activity began, the fitting uncertainty for the elastic strain components is  
26 estimated to introduce an uncertainty no greater than  $\pm 20\%$  on the measured CRSS values. These

1  
2  
3  
4     The elastic strain tensors were transformed to stress tensors using Hooke's Law with following  
5     elastic constants:  $C_{11}=162.4\text{GPa}$ ,  $C_{33}=181.6\text{GPa}$ ,  $C_{44}=47.2\text{GPa}$ ,  $C_{12}=92\text{GPa}$ ,  $C_{13}=69\text{GPa}$  [31].  
6  
7  
8  
9  
10

11     For a particular grain, this stress tensor, rather than the global uniaxial stress, was used to  
12     compute the resolved shear stresses for different slip systems. The above procedures were  
13     performed for all 37 deformation steps. To study the evolution of resolved shear stress, a key  
14     point is to track the same grains among different deformation steps. This is achieved by  
15  
16     considering both the crystallographic orientation and COM information: a grain in step ~~s~~ N and a  
17     grain in step ~~N+1~~ are recognized as the same grain if the difference of grain orientation is less  
18     than  $1^\circ$  and the distance between their COM is less than  $100\mu\text{m}$ . Due to the small strain step size  
19  
20     (less than 0.1% per step) and relatively large grain size, grain tracking was straightforward over  
21     all deformation steps. Among the 11 layers that correspond to a material volume of  
22  
23      $1.1\text{mm}\times1\text{mm}\times1\text{mm}$ , a total of 1153 grains were tracked and analyzed for their orientation,  
24  
25     rotation, and stress state evolution during sample loading. Grains that show continuous and  
26  
27     smooth changes in orientation are chosen for estimating the CRSS of slip modes.  
28  
29  
30  
31  
32  
33  
34  
35  
36  
37  
38  
39  
40

41     After the mechanical test, the sample was ~~taken out of removed from~~ the load frame, and a near-  
42     field HEDM scan was performed near the central part of the far-field measurement volume.  
43  
44     Near-field HEDM is able to yield spatially resolved 3D grain maps with much higher resolution  
45     ( $\sim 2\mu\text{m}$ ) than that provided by the COM [[3741–4044](#)]. The X-ray beam for the near-field scan  
46  
47     was  $4\mu\text{m}$  tall by 1.5mm wide with an energy of 64.3keV. The near-field X-ray area detector  
48  
49     (3mm $\times$ 3mm with  $2048\times2048$  pixels) was placed at distances of L=5.2 and 7.2 mm from the  
50  
51     rotation axis. The sample was rotated over a  $180^\circ$  range, and one diffraction image was collected  
52  
53     at each  $\delta\omega=1^\circ$  step for each L distance. By applying a forward modeling strategy [[3741–3943](#)],  
54  
55     the crystal orientation of each voxel in the scanned volume can be determined, which eventually  
56  
57  
58  
59  
60  
61  
62  
63  
64  
65

provides a spatially resolved grain map in the measured slice. The near-field scan was performed for 100 consecutive slices along the sample gauge length, which covered a material volume of  $400\mu\text{m} \times 1\text{mm} \times 1\text{mm}$ . Data reconstruction was performed for the top slice that resides in the 6th layer of the far-field scan.

### 3. Results

Figure 2 shows the  $\{0001\}$  pole figure and the COM map for the 104 indexed grains in layer 6 (the middle layer) before deformation. The  $\{0001\}$  texture is evident as most grains have their  $\{0001\}$  pole close to the Z direction (tensile axis). The grain COM map is consistent with the sample cross section dimension ( $1\text{mm} \times 1\text{mm}$ ) and the estimated grain size ( $\sim 100\mu\text{m}$ ). We previously examined A previous examination of the nucleation and evolution of a T1 twin nucleation event in Grain 1 at 1.6% strain is reported in [32]. For most other grains, dislocation slip was the dominant deformation mechanism-of deformation, which is the focus of this paper.

Figure 2 highlights 17 grains that were tracked in most of the 30 loading steps. They are identified with color coded markers that indicate the predominant slip activity in each of them, based upon the analysis strategy described next.

#### 3.1 Grains with predominant prismatic slip

During the tensile test, grain orientations gradually changed as a result of deformation. For the same grain, the difference in crystallographic orientation between step 1 and each subsequent step, after excluding the effect of symmetry, is calculated as the disorientation value at that step relative to step 1. The angular difference in the grain  $\langle 0001 \rangle$  direction between step 1 and each subsequent step is calculated as the c-axis misalignment at that step. Mathematically, the c-axis misalignment of a grain should not exceed its disorientation at any step.

Figure 3 shows the development of disorientation and c-axis misalignment with respect to the initial grain orientation (before deformation) for Grains 90, 95, 99, and 101. The disorientation and c-axis misalignment increased by almost ~~by~~ the same amount in each grain during early elastic deformation up to ~0.3% ~~engineering macroscopic~~ strain; ~~this which is probably likely~~ the result of ~~some small sample~~ a slight rotation of the whole sample (< 0.5°) prior to yielding.

After that, the disorientation continued to increase (up to 2.5°) with strain, but concurrently the c-axis misalignment from its initial orientation shows relatively small changes. This indicates that the majority of the grain rotation was around the c-axis during the plastic stage, which is evidence of prismatic slip activity. For each grain, the orientation difference between the last loading step and a step near the yield point (marked by the two arrows) is also annotated in each figure as  $\theta_{\text{rot}}$ , expressed in a rotational angle ~~-&~~ axis convention [4145]. The rotational axis is defined with respect to the crystal orthogonal coordinate system ( $\mathbf{x}_1, \mathbf{x}_2, \mathbf{x}_3$ ) illustrated in the large hexagonal unit cell in Figure 3. For all 4 grains, the rotational axis has a very large component along  $\mathbf{x}_3$ , which confirms the dominance of prismatic slip activity. From the {0001} pole figure in Figure 2(a), these 4 grains are all soft grains whose c-axis is almost perpendicular to the tensile direction Z, making it easy for prismatic slip to be activated. Figure 3 also plots the evolution of the von Mises stress calculated from the stress tensor:

$$\sigma_{VM} = \sqrt{\frac{(\sigma_{11} - \sigma_{22})^2 + (\sigma_{22} - \sigma_{33})^2 + (\sigma_{33} - \sigma_{11})^2 + 6(\sigma_{12}^2 + \sigma_{23}^2 + \sigma_{31}^2)}{2}}$$

For each grain, when the disorientation and the c-axis misalignment started to separate, the von Mises stress concurrently began to plateau. This shows a strong correlation between the activation of prismatic slip and grain yielding.

From the stress tensor, the resolved shear stress (RSS) on any slip system can be calculated.

Figure 4 shows the RSS on the most stressed prismatic slip system ( $\tau_{\text{prism}}$ ), basal slip system ( $\tau_{\text{basal}}$ ), and pyramidal  $\langle c+a \rangle$  slip system ( $\tau_{\langle c+a \rangle}$ ) in Grains 90, 95, 99, and 101 as a function of the macroscopic strain. Evolution of  $\tau_{\text{prism}}$  is generally smooth: it increased in early deformation prior to yield, then stabilized around a certain value for the rest of the loading steps. This is typical flow behavior for a grain deforming by a single dislocation slip, where no hardening takes place. For each grain, it is assumed that the strain increment when its disorientation deviated from the corresponding c-axis misalignment (see Figure 3) marks the activation of the most stressed prismatic slip system (in all cases, that system has the highest macroscopic-global Schmid factor assuming uniaxial tension along Z). For example, prismatic slip  $(01\bar{1}0)[\bar{2}110]$  (Schmid factor = 0.44) was activated in Grain 90 (Bunge Euler angles  $(\varphi_1, \Phi, \varphi_2) = (4.2^\circ, 70.3^\circ, 42.3^\circ)$ ) when the engineering-macroscopic strain was 0.14%, and the instantaneous  $\tau_{\text{prism}}$  was 105MPa.  $\tau_{\text{prism}}$  at this moment can be taken as the estimated CRSS for prismatic slip in Grain 90. The instantaneous  $\tau_{\text{basal}}$  and  $\tau_{\langle c+a \rangle}$  as well as the von Mises stress ( $\sigma_{\text{VM}}$ ) are also indicated in Figure 4. Note that  $\tau_{\text{prism}}$  is lower than both  $\tau_{\text{basal}}$  and  $\tau_{\langle c+a \rangle}$  when prismatic slip was activated, indicating that the prismatic slip mode has a lower CRSS than either basal slip and pyramidal  $\langle c+a \rangle$  slip. The same calculations were performed for Grains 95, 99, and 101, in which the CRSS for prismatic slip are found to be 90MPa, 112MPa, and 94MPa, respectively.

After searching for similar grain rotation behavior in all eleven layers, predominant prismatic slip was identified in a total of 18 grains (out of 1153 grains in the population). This number is small relative to the total number of grains for two reasons: (1) the texture of the sample is generally unfavorable for prismatic slip; (2) we only count those grains whose orientation rotation

1  
2  
3  
4 apparently resulted from prismatic slip were counted, and exclude the while more ambiguous  
5 cases were excluded. Figure 5 shows the distribution of CRSS for prismatic slip in these 18  
6 grains. The average and standard deviation CRSS for prismatic slip is  $96 \pm 18$  MPa, with most  
7 instances falling into the 70–110 MPa range.  
8  
9  
10  
11  
12  
13  
14  
15

### 16 *3.2 Grains with predominant basal slip*

### 17

18 Figure 6 shows the lattice rotation behavior and von Mises stress evolution for Grains 2, 5, 29,  
19 and 69 in the same way as in Figure 3. In these grains, the increase of c-axis misalignment was  
20 almost equal to the increase of disorientation throughout the loading. Hence, the grain rotation  
21 was mainly achieved by gradually tilting the c-axis, as illustrated by the large hexagonal unit cell  
22 in Figure 6. This behavior most likely results from basal slip, whose activation only tilts the c-  
23 axis of the crystal without causing any rotation around the c-axis. For each grain, the orientation  
24 change between the last loading step and a step near the yield point (marked by the two arrows)  
25 are also shown in the figure as  $\theta_{\text{rot}}$ . Theoretically, activation of a single basal slip system should  
26 make the crystal rotate around one of the  $<10\bar{1}0>$  directions. For example, activation of  
27  
28 (0001)[1 $\bar{2}$ 10] would cause lattice rotation around [10 $\bar{1}$ 0], which corresponds to the direction of  
29 [0.866, 0.5, 0] in the orthogonal crystal coordinate system ( $\mathbf{x}_1, \mathbf{x}_2, \mathbf{x}_3$ ). The observed rotation axis  
30 for Grain 2, Grain 29, and Grain 69 are generally close to this type of theoretical direction. From  
31 the observed rotation axis in Grain 2 ( $\varphi_1, \Phi, \varphi_2 = 81.6^\circ, 7.7^\circ, 39.4^\circ$ ), it is inferred that  
32  
33 (0001)[11 $\bar{2}$ 0] basal slip with a global Schmid factor of 0.13 was activated. Similar calculations  
34 are performed for Grains 29 and 69, where the identified active basal slip systems had global  
35 Schmid factor of 0.35 and 0.19, respectively. For Grain 5 ( $\varphi_1, \Phi, \varphi_2 = 28.3^\circ, 18.3^\circ, 43.9^\circ$ ), the  
36  
37  
38  
39  
40  
41  
42  
43  
44  
45  
46  
47  
48  
49  
50  
51  
52  
53  
54  
55  
56  
57  
58  
59  
60  
61  
62  
63  
64  
65

1  
2  
3  
4  
5 rotation axis is close to [2 $\bar{1}\bar{1}0$ ], which could be achieved by the simultaneous operation of two  
6  
7 basal slip systems (0001)[1 $\bar{2}10$ ] (~~global Schmid factor=0.20~~) and (0001)[11 $\bar{2}0$ ] (global Schmid  
8 factors of 0.20 and =0.29, respectively).  
9  
10  
11  
12  
13  
14  
15

16 Figure 7 shows the RSS on the most stressed prismatic slip system ( $\tau_{\text{prism}}$ ), basal slip system  
17 ( $\tau_{\text{basal}}$ ), and pyramidal  $<\text{c+a}>$  slip system ( $\tau_{<\text{c+a}>}$ ) in Grains 2, 5, 29, and 69 as a function of the  
18 macroscopic strain. For Grain 2, Grain 29, and Grain 69, the activated basal slip systems inferred  
19 from lattice rotation are in fact the most stressed basal slip system (i.e. highest RSS). For Grain 5,  
20  
21 (0001)[11 $\bar{2}0$ ] is the most stressed basal slip system. In all four cases,  $\tau_{\text{prism}}$  is lower than the  
22 lowest CRSS value of 69 MPa identified above for prismatic slip to be activated. Because the  
23 overall disorientation as well as the c-axis misalignment changed continuously through the test, it  
24 is not obvious when basal slip was first activated in as clear of a way as that shown in Figure 3  
25 for prismatic slip (i.e. deviation of disorientation from c-axis misalignment). As an alternative  
26 criterion, it is we assumed that basal slip was activated when the von Mises stress ( $\sigma_{\text{VM}}$ ) began to  
27 plateau. Under this assumption, the CRSS values for basal slip were calculated for each grain  
28 and shown in Figure 7 along with the instantaneous  $\tau_{\text{basal}}$ ,  $\tau_{<\text{c+a}>}$ , and  $\sigma_{\text{VM}}$ . The CRSS for basal  
29 slip is apparently higher than the values above determined value for prismatic slip.  
30  
31  
32  
33  
34  
35  
36  
37  
38  
39  
40  
41  
42  
43  
44  
45  
46  
47  
48  
49  
50  
51  
52  
53  
54  
55  
56  
57  
58  
59  
60  
61  
62  
63  
64  
65

Grain 29 is a good example to show that use of the local stress tensor to obtain the RSS is a more reliable parameter to predict slip activity than the global Schmid factor: when the basal slip was activated,  $\tau_{\text{prism}}$  and  $\tau_{\text{basal}}$  were 61MPa and 135MPa, but the global Schmid factor for the two slip systems (~~assuming uniaxial tension along Z~~) were equal ( $\sim 0.35$ ). From the global Schmid factor,

1  
2  
3  
4 one would expect prismatic slip to be activated; but from the measured RSS, basal slip was  
5  
6 **actually clearly** favored over prismatic slip in this grain, consistent with the observation.  
7  
8  
9  
10

11 Though  $\tau_{c+a}$  reached 245MPa, 243MPa, and 242MPa in Grains 2, 5, and 69 by the time basal  
12 slip was activated, it appears that pyramidal  $c+a$  slip was not activated in a dominant way.  
13 Had pyramidal  $c+a$  dominated, the absolute value of the  $x_3$  component of the rotation axis  
14 would be close to 0.23, a value at least two times greater than the observed absolute value of the  
15  $x_3$  component in all four grains. This suggests that the CRSS of pyramidal  $c+a$  slip is likely no  
16 less than 240MPa. On the other hand, the fact that the  $x_3$  component is non-zero suggests that  
17 pyramidal  $c+a$  might have occurred as secondary slip. Grain 2 and Grain 69 had relatively  
18 high ratio of  $\tau_{c+a} / \tau_{\text{basal}}$  (~2.3 and ~2.1) whereas this ratio in Grain 5 and Grain 29 ~~is-were~~ ~1.6  
19 and ~0.8). Activation of pyramidal  $c+a$  slip in addition to basal slip might be that reason that  
20 the observed rotation axes show a relatively large  $x_3$  component in Grain 2 and Grain 69  
21 compared with Grain 5 and Grain 29.  
22  
23  
24  
25  
26  
27  
28  
29  
30  
31  
32  
33  
34  
35  
36  
37  
38  
39  
40

41 After searching for similar grain rotation behavior in all the eleven layers, predominant basal slip  
42 was identified in a total of 22 grains. The distribution of CRSS for basal slip in these 22 grains is  
43 shown in Figure 5. The average CRSS for basal slip is  $127 \pm 33$  MPa.  
44  
45  
46  
47  
48  
49  
50  
51  
52

### 3.3 *Grains with weak or complicated slip activity*

53 While the 8 grains analyzed above appear to be dominated by the activation of a single slip  
54 system, this is not always the case for ~~many-most~~ other grains. Figure 8 shows the development  
55 of disorientation and c-axis misalignment with strain for nine grains, in which it is difficult to  
56 identify a dominant slip system with confidence. For Grains 4, 36, and 47, the lattice rotation  
57  
58  
59  
60  
61  
62  
63  
64  
65

1  
2  
3  
4 was relatively small, suggesting weak slip activity. Such a change in the orientation may have  
5 arisen from rigid body motion imposed by deformation in neighboring grains. For Grains 12, 14,  
6 and 91, the c-axis misalignment and the disorientation change in an increase-decrease-increase  
7 manner. This complicated path of lattice rotation may have arisen from simultaneous operation  
8 of two slip systems at varying rates whose associated lattice rotation were partially canceled out  
9 from each other. For Grains 60, 61, and 65, the disorientation was higher than the c-axis  
10 misalignment during early deformation, but then the difference gradually shrank during later  
11 deformation. This scenario suggests a change in the dominant slip system with increasing strain  
12 in these grains. Figure 9 shows the evolution of  $\tau_{\text{prism}}$ ,  $\tau_{\text{basal}}$ , and  $\tau_{<\text{c+a}>}$  in the ~~above same~~ nine  
13 grains. Grains 12, 14, 91, 60, 61 and 65 all had  $\tau_{\text{basal}}$  (RSS on the most stressed basal slip system)  
14 exceeding 140MPa after grain yielding. Given the previously determined average CRSS for  
15 basal slip (127MPa), it is likely that basal slip was activated in these grains. The RSS on the  
16 second most stressed basal slip system also exceeded 120MPa in each of the 6 grains at some  
17 point. The RSS on the most stressed prismatic slip system exceeded 70MPa in Grains 12, 14, and  
18 91. When multiple slip systems were activated in a grain at different strains and in different  
19 regions, a complex path of grain rotation can be expected.

#### 46 *3.4 Grain-level residual stress and stress heterogeneity*

47 *Figure 10 (a-c) show the von Mises stress ( $\sigma_{\text{VM}}$ ) development at macroscopic strains of 0, 0.31%,*  
48 *and 2.6% in all grains in layer 6. Prior to the deformation,  $\sigma_{\text{VM}}$  varies from 50 to 200MPa in*  
49 *different grains (Figure 10(a)). This indicates the existence of residual stress in the initial state,*  
50 *which was probably due to the anisotropic thermal contraction of Ti during cooling after a*  
51 *recrystallization anneal. After the tensile test started,  $\sigma_{\text{VM}}$  in those grains increased and became*  
52 *more and more heterogeneous among different grains (Figure 10(b,c)). This grain-level stress*

1  
2  
3  
4 heterogeneity is the result of the heterogeneous deformation paths among different grains. Figure  
5  
6 10(d) compares the average von Mises stress among all grains in layer 6 with the macroscopic  
7 tensile stress applied on the sample. The two values were very similar throughout the loading.  
8  
9 Upon unloading, residual stresses emerged again in many grains even after the macroscopic  
10 stress on the sample was fully removed. The average von Mises stress was 160MPa at the final  
11 unload step. This post-deformation residual stress can be attributed to the “internal stresses”  
12 between neighboring grains that developed during deformation and unloading.  
13  
14

15  
16  
17  
18  
19 3.4.5 Grain map from the near-field HEDM scan  
20  
21

22  
23 After the in situ far-field HEDM, a near-field HEDM scan was performed in approximately the  
24 same region of the sample. Near-field HEDM provides a non-destructive planar mapping of the  
25 detailed arrangement of grains in the microstructure similar to the more familiar electron back-  
26 scatter diffraction (EBSD) scans. The original purpose for the near-field HEDM was to further  
27 examine twin nucleation from the in situ far-field HEDM measurement. (Among the 1153 grains,  
28 twin nucleation was identified in 19 grains by far-field HEDM.) The near-field HEDM data  
29 allow the exploration of the morphology and location of the nucleated twins with respect to other  
30 microstructurally-relevant features such as grain boundaries and the spatial arrangement of hard  
31 versus soft grains, but this is beyond the scope of the present paper.  
32  
33  
34  
35  
36  
37  
38  
39  
40  
41  
42  
43  
44  
45  
46  
47  
48  
49

50 Figure 1011(a) shows the grain map from the top slice of the near-field HEDM scan, which was  
51 found to be located in the 6th layer of the far-field scan. The pixel size for the reconstruction was  
52 set to be 2 $\mu$ m, and the grains are colored randomly. Each grain is colored according to the angle  
53 between its c-axis and the Z direction: if that angle is 0, the grain is colored towards red (hard-  
54 oriented grain); if that angle c-axis is 90°, the grain is colored towards blue (soft-oriented grain).  
55  
56  
57  
58  
59  
60  
61  
62  
63  
64  
65

1  
2  
3  
4 Figure 1011(b) shows the corresponding {0001} pole figure for the grains in the near-field map.  
5  
6  
7  
8  
9

10  
11 are identified in the near-field grain map based on the match of both grain position and grain  
12 orientation. Comparing Figure 10-11 and Figure 2, the grain COMs match very well are similar  
13 between the near-field and far-field results, but there is no reason to expect them to be the same,  
14 as the near field measurement samples a thin slice rather than the entire volume of the grain.  
15  
16

17 Grain orientations are generally consistent, but some differences still exist between the near-field  
18 and far-field grain orientations. This difference is plausible and could result from sample  
19 mounting: the near-field scan was performed after the sample was taken out of the load frame and  
20 glued onto another stage; it is very difficult to guarantee that the sample was remounted exactly  
21 the same way as it was in the load cell. Grains 29, 60, 36 and 99 are absent in the near-field scan  
22  
23 grain map. One possibility of their absence is, which likely implies that these grains did not  
24 intersect the near-field scan slice (4 $\mu\text{m}$  tall) measured slice but are present elsewhere in the  
25  
26 100 $\mu\text{m}$  much thicker layer 6 of the far-field scan (100 $\mu\text{m}$  tall).  
27  
28  
29  
30  
31  
32  
33  
34  
35  
36  
37  
38  
39  
40

## 4. Discussion

### 4.1 CRSS ratio between basal slip and prismatic slip

41 From Sections 3.1 and 3.2, the CRSS values for prismatic slip and basal slip are in the range of  
42  
43 96 $\pm$ 18 MPa and 127 $\pm$ 33 MPa, respectively, in this material. Our previous work showed that the  
44 T1 twin in Grain 1 nucleated at a RSS of 225MPa [32]. Although the CRSS for pyramidal <c+a>  
45  
46 slip is not directly determined from this study, it is likely no less probably greater than 240MPa  
47  
48 from the above analysis. These results are listed in the last row in Table 1 for comparison with  
49  
50 the literature values.  
51  
52  
53  
54  
55  
56  
57  
58  
59  
60  
61  
62  
63  
64  
65

The ratio of  $\text{CRSS}_{\text{basal}}/\text{CRSS}_{\text{prism}}$  is particularly important for the ductility of hexagonal metals. A ratio that is not too far from 1.0 allows both prismatic and basal slip to be activated during material deformation, which is beneficial for the material ductility. ~~A simple practice that divides~~  
~~Simply dividing~~ the average CRSS ~~values (127MPa for basal slip, 96MPa for prismatic slip) (i.e. 127MPa)~~ by the average CRSS of prismatic slip (i.e. 96MPa), however, is not an accurate way to estimate this ratio of  $\text{CRSS}_{\text{basal}}/\text{CRSS}_{\text{prism}}$ . Instead, ~~we use the instantaneous values of  $\tau_{\text{prism}}$  and  $\tau_{\text{basal}}$  at the onset of the dominant mode in each relevant grain for the 18 grains that show prismatic slip and the 22 grains that show basal slip are used~~ to estimate the upper and lower ~~boundaries bounds~~ for the ratio of  $\text{CRSS}_{\text{basal}}/\text{CRSS}_{\text{prism}}$ . This method effectively eliminates the influence of grain size and neighboring grains. To some extent, it is equivalent to conducting slip activity analysis for 40 single crystals with different orientations. The result is summarized in Figure 12. ~~for Of~~ the 18 grains that show prismatic slip, 17 ~~of them~~ have  $\tau_{\text{basal}}/\tau_{\text{prism}}$  less than 2.1. In other words, prismatic slip ~~can be theis~~ dominant ~~slip mode~~ only when  $\tau_{\text{basal}}/\tau_{\text{prism}}$  is less than 2.1. For the 22 grains that show basal slip, all ~~of them~~ have  $\tau_{\text{basal}}/\tau_{\text{prism}}$  greater than 1.7. In other words, basal slip ~~can be theis~~ dominant ~~slip mode~~ only when  $\tau_{\text{basal}}/\tau_{\text{prism}}$  is greater than 1.7. ~~Combining the above boundaries~~ Thus, we estimate the ratio of  $\text{CRSS}_{\text{basal}}/\text{CRSS}_{\text{prism}}$  is between 1.7 and 2.1 for this Ti material. This range is in the middle of the reported values in the literature (see Table 1).

~~From the grain COM positions, it is possible to distinguish grains with a free surface (i.e. surface grains) from grains in the interior volume (i.e. inner grains). From Figure 12, this has no apparent influence on the CRSS ratio, but free surface effects are discussed further in the next section.~~

1  
2  
3  
4 ***4.2 Effects of grain size and free surface on slip activity Reasons for the variation of the CRSS***  
5  
6  
7  
8  
9

## values

10 From Figure 5, the CRSS for both prismatic slip and basal slip have a broad range. The variation  
11 of CRSS from grain to grain may be attributed to ~~a few possibl~~~~e several~~ factors. First of all, the  
12 stress tensor in each grain was determined from its elastic strain tensor, which is fitted using all  
13 identified peaks of that grain. As discussed in Section 2, the fitting procedure itself is associated  
14 with some intrinsic uncertainty. Second, First, the stress state could be heterogeneous within a  
15 grain, but the stress tensor obtained from the far-field measurement is a grain-averaged value.  
16 Local stress within a grain, however, often deviates from the grain-averaged stress particularly  
17 near grain boundaries. This could result in an underestimation of the CRSS in some grains in  
18 which dislocation slip was initiated in a region where the local stress was substantially higher  
19 than the grain-averaged stress. Unfortunately, it is difficult to examine the stress ~~heterogeneity~~  
20 ~~factor localization~~ with ~~the current~~ far-field data. The third factor is the influence of neighboring  
21 grains. Many studies have shown that dislocation slip or twinning in one grain could stimulate  
22 the activation of slip or twins in the neighboring grain through slip transfer, should the two  
23 deformation systems have a good geometric alignment with each other [5, 8, 44, 46, 47]. Again,  
24 it is not straightforward to assess this issue with the far-field data that cannot provide accurate  
25 grain morphology information. The ~~Grain~~ grain size and free surface are two other factors that  
26 could explain account for the variation of the CRSS values. These two factors are examined in  
27 detail in Figure 13. We examine how these two effects would affect the CRSS value and show the  
28 result in Figure 12. For each grain, its grain size is estimated to be the distance from its COM to  
29 the COM of its 3<sup>rd</sup> closest neighboring grain. (The average grain size from this estimation is  
30 103 $\mu\text{m}$ , very close to the ~~known previously measured~~ grain size ( $\sim 100\mu\text{m}$ ) of this material [12].)  
31 From the grain COM map, each grain is classified as either a surface grain if its COM is adjacent  
32 to a free surface or an interior grain if its COM is adjacent to another grain. The grain size  
33 and free surface classification are used to further investigate the variation of the CRSS values  
34 in the next section. Finally, we examine the effect of the free surface on the CRSS values.  
35 We find that the CRSS values for grains near the free surface are significantly lower than those  
36 farther away from the free surface. This is likely due to the fact that the free surface provides  
37 a low-friction boundary for dislocation slip, which can lead to a reduction in the CRSS value.  
38 Overall, we find that the variation of the CRSS values is influenced by multiple factors, including  
39 grain size, free surface, and neighboring grains. By examining these factors, we gain a better  
40 understanding of the mechanical behavior of the material at the microscale.

1  
2  
3  
4 to one of the four surface edges or an inner grain if otherwise. Figure 4213(a) compares the  
5 CRSS and the grain size of the 18 grains that show prismatic slip. Nine of ~~them~~these are surface  
6 grains and the others are inner grains. It appears that the CRSS for prismatic slip ~~to occur in a~~  
7 ~~grain~~ is negatively correlated with the grain size. The average CRSS values~~s~~ for prismatic slip in  
8 the nine surface grains and the nine inner grains are  $91 \pm 19$  MPa and  $102 \pm 16$  MPa, respectively.  
9  
10 A statistical analysis using the Standard t-test indicates that the probability for the alternative  
11 hypothesis  $H_1 = \{\text{CRSS}_{\text{surface grains}} < \text{CRSS}_{\text{inner grains}}\}$  to be valid is 0.88. Figure 4213(b) compares  
12 the CRSS and the grain size of the 22 grains that show basal slip. Again, it appears that the  
13 CRSS for basal slip to occur in a grain is negatively correlated with the grain size. The average  
14 CRSS value for basal slip in the eight surface grains and the fourteen inner grains are  $105 \pm 25$   
15 MPa and  $139 \pm 31$  MPa, respectively. Standard-The same t-test indicates that the probability for  
16 the alternative hypothesis  $H_1 = \{\text{CRSS}_{\text{surface grains}} < \text{CRSS}_{\text{inner grains}}\}$  to be valid is as high as 0.99.  
17  
18

19 From Figure 4213, it is concluded that both the grain size and the free surface will affect the  
20 CRSS for slip activity. Larger grains generally require less resolved shear stress for prismatic or  
21 basal slip to be activated, which agrees with the Hall-Petch relation. Grains adjacent to the free  
22 surface also require less resolved shear stress for prismatic or basal slip to be activated compared  
23 with grains in the interior volume. This finding suggests that the common practice of using the  
24 surface slip activity characterized by SEM to represent the behavior of the bulk material must be  
25 taken with some caution. When simulating the mesoscale plastic deformation of polycrystalline  
26 materials with full field crystal plasticity frameworks such as crystal plasticity finite element  
27 modeling (CPFEM) [42] and Fast Fourier Transformation (FFT) [43], it may be necessary to  
28 assign different CRSS values for surface grains and for inner grains, especially when the sample  
29 size is small and surface grains account for a relatively large volume fraction of the sample.  
30  
31

1  
2  
3  
4  
5  
6 Experimental measurement of CRSS of different slip modes provides important parameters for  
7 crystal plasticity modeling. In this paper, analysis of a material volume of  $1.1\text{mm} \times 1\text{mm} \times 1\text{mm}$   
8 of the far-field HEDM measurement was made to identify enough grains with dominant prismatic  
9 slip and basal slip to estimate the CRSS for these two slip modes. A 3D grain structure  
10 reconstruction using the information of all 11 layers and Voronoi tessellation for subsequent  
11

12 CPFEF crystal plasticity simulation has been constructed, and will be the basis for future  
13 assessments of heterogeneous deformationis under way. The CRSS values obtained from the  
14 present work will become provide important the input parameters, and the accurately measured  
15 grain orientation change during loading will serve as a good benchmark to assess the quality of  
16 the model itself.  
17  
18

## 30 31 32 33 34 35 36 37 38 39 40 41 42 43 44 45 46 47 48 49 50 51 52 53 54 55 56 57 58 59 60 61 62 63 64 65 5. Conclusions

In situ far-field HEDM was used to track the deformation history of individual grains in a bulk Ti polycrystalline sample deformed up to 2.6% tensile strain. Deformation history in a total of 1158 grains were analyzed with a focus on those grains that show predominant activity of either prismatic slip or basal slip. The following conclusions are reached:

1. Prismatic slip was found in 18 grains, whose lattice rotationss was-were mostly around the c-axis. Assuming that prismatic slip was activated when the disorientation started to deviate from c-axis misalignment in each grain, the average CRSS for prismatic slip was estimated to be  $96 \pm 18$  MPa.
2. Basal slip was found in 22 grains, whose lattice rotationss was-were predominantly observed througha tilting of the c-axis about an axis in the basal plane. Assuming that basal slip was

1  
2  
3  
4 activated when the grain-averaged von Mises stress began to plateau, the average CRSS for basal  
5 slip was estimated to be  $127 \pm 33$  MPa. The CRSS for pyramidal  $\langle c+a \rangle$  slip systems, for which  
6  
7 no examples were observed, is likely no lessapparently greater than 240MPa.  
8  
9  
10

11 3. Not all grains show simple slip activity. Instead, many the majority of the grains show either  
12 small or complicated lattice rotations. The latter can be attributed to the activation of multiple  
13 slip systems within a grain.  
14  
15

16 4. An ex situ post-deformation near-field HEDM scan allows visualization of the detailed  
17 arrangement of grainsshape of some grains in the 6th layer of the far-field scan. This provided  
18 confirmation of the locations and credibility of geometric COM values extracted from far-field  
19 measurements.  
20  
21

22 5. The ratio of  $\text{CRSS}_{\text{basal}}/\text{CRSS}_{\text{prism}}$  is estimated to be between 1.7 and 2.1 for this commercial  
23 purity Ti material.  
24  
25

26 6. The observed variation of CRSS values for both prismatic slip and basal slip can be attributed  
27 to a number of factors, such as the intrinsic fitting uncertainty of the stress tensor, in-grain stress  
28 inhomogeneity, slip transfer from neighboring grains, grain size, and the influence of the free  
29 surface. Examination of the last two factors shows that the CRSS for slip isare negatively  
30 correlated with the grain size. Also, grains adjacent to the free surface show lower CRSS for slip  
31 to be activated compared with grains from the interior of the material.  
32  
33  
34

## 50 Acknowledgements

51  
52

53 This work was supported by NSF Materials World Network grants NSF-DMR-1108211 and  
54 DMR-0710570 at Michigan State University. Work at Carnegie Mellon University was  
55 supported by the U.S. Department of Energy under Award DESC0002001. Use of the Advanced  
56 Photon Source was supported by the United States Department of Energy, Office of Science,  
57  
58  
59  
60  
61  
62  
63  
64  
65

1  
2  
3  
4 Office of Basic Energy Sciences, under Contract No. DE-AC02-06CH11357. LW acknowledges  
5 the support of the National Natural Sciences Foundation of China (No. 51671127). JL was partly  
6 supported by Lawrence Livermore National Laboratory under contract DE-AC52-07NA27344.  
7  
8 RMS received support through the Visiting Scientist program of the X-Ray Science Division,  
9 Argonne National Laboratory. The authors are grateful for the support from Jonathan Almer and  
10 Ali Mashayekhi of APS Beamline 1-ID during the beamtime. We thank Armand Beaudoin for  
11 his help with the Matlab code for far-field data analysis. JL and RMS also thank Shiu Fai Li for  
12 many helpful conversations and for his implementation of the forward modeling, near-field  
13 reconstruction code.  
14  
15  
16  
17  
18  
19  
20  
21  
22  
23

## 25 26 27 28 **References** 29 30

- 31 [1] J.J. Fundenberger, M.J. Philippe, F. Wagner, C. Esling, Modelling and prediction of  
32 mechanical properties for materials with hexagonal symmetry (zinc, titanium and zirconium  
33 alloys), *Acta Mater.* 45 (1997) 4041–4055.  
34  
35 [2] X. Tan, H. Guo, H. Gu, C. Laird, N.D.H. Munroe, Cyclic deformation behavior of high-purity  
36 titanium single crystals: Part II. Microstructure and mechanism, *Metall. Mater. Trans. A* 29 (1998)  
37 513–518.  
38  
39 [3] M.H. Yoo, Slip, twinning, and fracture in hexagonal close-packed metals, *Metall. Trans. A* 12  
40 (1981) 409–418.  
41  
42 [4] F. Bridier, P. Villechaise, J. Mendez, Analysis of the different slip systems activated by  
43 tension in a  $\alpha/\beta$  titanium alloy in relation with local crystallographic orientation, *Acta Mater.* 53  
44 (2005) 555–567.  
45  
46  
47  
48  
49  
50  
51  
52  
53  
54  
55  
56  
57  
58  
59  
60  
61  
62  
63  
64  
65

- [5] L. Wang, Y. Yang, P. Eisenlohr, T.R. Bieler, M.A. Crimp, D.E. Mason, Twin Nucleation by Slip Transfer across Grain Boundaries in Commercial Purity Titanium, *Metall. Mater. Trans. A* 41 (2010) 421–430.
- [6] S. Zaefferer, A study of active deformation systems in titanium alloys: dependence on alloy composition and correlation with deformation texture, *Mater. Sci. Eng. A* 344 (2003) 20–30.
- [7] H. Li, D.E. Mason, T.R. Bieler, C.J. Boehlert, M.A. Crimp, Methodology for estimating the critical resolved shear stress ratios of  $\alpha$ -phase Ti using EBSD-based trace analysis, *Acta Mater.* 61 (2013) 7555–7567.
- [8] B. Barkia, V. Doquet, J.P. Couzinié, I. Guillot, E. Héripé, In situ monitoring of the deformation mechanisms in titanium with different oxygen contents, *Mater. Sci. Eng. A* 636 (2015) 91–102.
- [9] J.C. Schuren, P.A. Shade, J.V. Bernier, S.F. Li, B. Blank, J. Lind, P. Kenesei, U. Lienert, R.M. Suter, T.J. Turner, D.M. Dimiduk, J. Almer, New opportunities for quantitative tracking of polycrystal responses in three dimensions, *Curr. Opin. Solid State Mater. Sci.* 19 (2015) 235–244.
- [10] A.A. Salem, S.R. Kalidindi, S.L. Semiatin, Strain hardening due to deformation twinning in  $\alpha$ -titanium: Constitutive relations and crystal-plasticity modeling, *Acta Mater.* 53 (2005) 3495–3502.
- [11] X. Wu, S.R. Kalidindi, C. Necker, A.A. Salem, Prediction of crystallographic texture evolution and anisotropic stress-strain curves during large plastic strains in high purity  $\alpha$ -titanium using a Taylor-type crystal plasticity, *Acta Mater.* 55 (2007) 423–432.
- [12] L. Wang, R.I. Barabash, Y. Yang, T.R. Bieler, M.A. Crimp, P. Eisenlohr, W. Liu, G.E. Ice, Experimental Characterization and Crystal Plasticity Modeling of Heterogeneous Deformation in Polycrystalline alpha-Ti, *Metall. Mater. Trans. A* 42 (2011) 626–635.

- [13] Y. Yang, L. Wang, T.R. Bieler, P. Eisenlohr, M.A. Crimp, Quantitative Atomic Force Microscopy Characterization and Crystal Plasticity Finite Element Modeling of Heterogeneous Deformation in Commercial Purity Titanium, *Metall. Mater. Trans. A* 42 (2011) 636–644.
- [14] J.L.W. Warwick, N.G. Jones, K.M. Rahman, D. Dye, Lattice strain evolution during tensile and compressive loading of CP Ti, *Acta Mater.* 60 (2012) 6720–6731.
- [15] M. Knezevic, R.A. Lebensohn, O. Cazacu, B. Revil-Baudard, G. Proust, S.C. Vogel, M.E. Nixon, Modeling bending of alpha-titanium with embedded polycrystal plasticity in implicit finite elements, *Mater. Sci. Eng. A* 564 (2013) 116–126.
- [16] D. Gloaguen, G. Oum, V. Legrand, J. Fajoui, S. Branchu, Experimental and theoretical studies of intergranular strain in an alpha titanium alloy during plastic deformation, *Acta Mater.*, 61 (2013) 5779–5790.
- [17] K.E.K. Amouzou, T. Richeton, A. Roth, M.A. Lebyodkin, T.A. Lebedkina, Micromechanical modeling of hardening mechanisms in commercially pure  $\alpha$ -titanium in tensile condition, *Int. J. Plasticity* 80 (2016) 222–240.
- [18] J. Gong, A.J. Wilkinson, Anisotropy in the plastic flow properties of single-crystal  $\alpha$  titanium determined from micro-cantilever beams, *Acta Mater.* 57(2009) 5693–5705.
- [19] J. Gong, A.J. Wilkinson, Micro-cantilever testing of  $\langle a \rangle$  prismatic slip in commercially pure Ti, *Philos. Mag.* 91 (2011) 1137–1149.
- [20] M. D. Uchic, D. M. Dimiduk, J. N. Florando, W. D. Nix, Sample dimensions influence strength and crystal plasticity, *Science*. 305 (2004) 986–989.
- [21] E.M. Lauridsen, S. Schmidt, R.M. Suter, H.F. Poulsen, Tracking: a method for structural characterization of grains in powders or polycrystals, *J. Appl. Crystallogr.* 34 (2001) 744–750.

- [22] H.F. Poulsen, S.F. Nielsen, E.M. Lauridsen, S. Schmidt, R.M. Suter, U. Lienert, L. Margulies, T. Lorentzen, D.J. Jensen, Three-dimensional maps of grain boundaries and the stress state of individual grains in polycrystals and powders, *J. Appl. Crystallogr.* 34 (2001) 751–756.
- [23] H.F. Poulsen, *Three-Dimensional X-ray Diffraction Microscopy*. Berlin: Springer; 2004.
- [24] H.F. Poulsen, An introduction to three-dimensional X-ray diffraction microscopy, *J. Appl. Crystallogr.* 45 (2012) 1084–1097.
- [25] L. Margulies, T. Lorentzen, H. F. Poulsen, T. Leffers, Strain tensor development in a single grain in the bulk of a polycrystal under loading, *Acta Mater.* 50(2002) 1771–1779.
- [26] R.V. Martins, L. Margulies, S. Schmidt, H.F. Poulsen, T. Leffers, Simultaneous measurement of the strain tensor of 10 individual grains embedded in an Al tensile sample, *Mater. Sci. Eng. A* 387 (2004) 84–88.
- [27] J.V. Bernier, N.R. Barton, U. Lienert, M.P. Miller, Far-field high-energy diffraction microscopy: a tool for intergranular orientation and strain analysis, *J. Strain Anal. Eng. Des.* 46 (2011) 527–547.
- [28] J. Oddershede, S. Schmidt, H.F. Poulsen, H.O. Sorensen, J. Wright, W. Reimers, Determining grain resolved stresses in polycrystalline materials using three-dimensional X-ray diffraction, *J. Appl. Crystallogr.* 43 (2010) 539–549.
- [29] J. Oddershede, B. Camin, S. Schmidt, L.P. Mikkelsen, H.O. Sorensen, U. Lienert, H.F. Poulsen, W. Reimers, Measuring the stress field around an evolving crack in tensile deformed Mg AZ31 using three-dimensional X-ray diffraction, *Acta Mater.* 60 (2012) 3570–3580.
- [30] C.C. Aydiner, J.V. Bernier, B. Clausen, U. Lienert, C.N. Tome, D.W. Brown, Evolution of stress in individual grains and twins in a magnesium alloy aggregate, *Phys. Rev. B* 80 (2009) 024113.

[31] T.R. Bieler, L.Y. Wang, A.J. Beaudoin, P. Kenesei, U. Lienert, In Situ Characterization of Twin Nucleation in Pure Ti Using 3D-XRD, Metall. Mater. Trans. A 45 (2014), 109–122.

[32] L. Wang, J. Lind, H. Phukan, P. Kenesei, J.-S. Park, R.M. Suter, A.J. Beaudoin, T.R. Bieler, Mechanical twinning and detwinning in pure Ti during loading and unloading - An in situ high-energy X-ray diffraction microscopy study, Scripta Mater. 92 (2014) 35–38.

[33] H. Abdolvand, M. Majkut, J. Oddershede, S. Schmidt, U. Lienert, B.J. Diak, P.J. Withers, M.R. Daymond, On the deformation twinning of Mg AZ31B: A three-dimensional synchrotron X-ray diffraction experiment and crystal plasticity finite element model, Int J Plasticity. 70 (2015) 77–97.

[34] H. Abdolvand, M. Majkut, J. Oddershede, J.P. Wright, M.R. Daymond, Study of 3-D stress development in parent and twin pairs of a hexagonal close-packed polycrystal: Part I – in-situ three-dimensional synchrotron X-ray diffraction measurement, Acta Mater. 93 (2015) 246–255.

[35] S.L. Wong, J.-S. Park, M.P. Miller, P.R. Dawson, A framework for generating synthetic diffraction images from deforming polycrystals using crystal-based finite element formulations, Comp. Mater. Sci. 77 (2013) 456–466.

[36] D.C. Pagan, M.P. Miller, Connecting heterogeneous single slip to diffraction peak evolution in high-energy monochromatic X-ray experiments, J. Appl. Crystallogr. 47 (2014) 887–898.

[37] T. Ungár, G. Ribárik, G. Zilahi, R. Mulay, U. Lienert, L. Balogh, S. Agnew, Slip systems and dislocation densities in individual grains of polycrystalline aggregates of plastically deformed CoTi and CoZr alloys, Acta Mater. 71 (2014) 264–282.

[38] J. Oddershede, J. P. Wright, A. Beaudoin, G. Winther, Deformation-induced orientation spread in individual bulk grains of an interstitial-free steel, Acta Mater. 85 (2015) 301–313.

- [3539] U. Lienert, S. F. Li, C. M. Hefferan, J. Lind, R. M. Suter, J. V. Bernier, N. R. Barton, M. C. Brandes, M. J. Mills, M. P. Miller, B. Jakobsen, W. Pantleon, High-energy diffraction microscopy at the advanced photon source, *JOM* 63 (2011) 70–77.
- [3640] S. Schmidt, GrainSpotter: a fast and robust polycrystalline indexing algorithm, *J. Appl. Crystallogr.* 47 (2014) 276–284.
- [3741] R.M. Suter, D. Hennessy, C. Xiao, U. Lienert, Forward modeling method for microstructure reconstruction using x-ray diffraction microscopy: Single-crystal verification, *Rev. Sci. Instrum.* 77 (2006) 123905.
- [3842] C.M. Hefferan, S.F. Li, J. Lind, U. Lienert, A.D. Rollett, P. Wynblatt, R.M. Suter, Statistics of High Purity Nickel Microstructure From High Energy X-ray Diffraction Microscopy, *Comput. Mat. Contin.* 14 (2009) 209–219.
- [3943] S.F. Li, R.M. Suter, Adaptive reconstruction method for three-dimensional orientation imaging, *J. Appl. Crystallogr.* 46 (2013) 512–524.
- [4044] J. Lind, S.F. Li, R. Pokharel, U. Lienert, A.D. Rollett, R.M. Suter, Tensile twin nucleation events coupled to neighboring slip observed in three dimensions, *Acta Mater.* 76 (2014) 213–220.
- [4145] U.F. Kocks, C.N. Tomé, H.R. Wenk, *Texture and anisotropy*. Cambridge: Cambridge University Press; 2000.
- [46] Y. Guo, T. B. Britton, A. J. Wilkinson, Slip band–grain boundary interactions in commercial-purity titanium, *Acta Mater.* 76 (2014) 1–12.
- [47] L. Nervo, A. King, A. Fitzner, W. Ludwig, M. Preuss, A study of deformation twinning in a titanium alloy by X-ray diffraction contrast tomography, *Acta Mater.* 105 (2016) 417–428.
- [42] F. Röters, P. Eisenlohr, L. Hantcherli, D. D. Tjahjanto, T. R. Bieler, D. Raabe, Overview of constitutive laws, kinematics, homogenization and multiscale methods in crystal plasticity finite-element modeling: Theory, experiments, applications, *Acta Mater.* 58 (2010) 1152–1211.

[43] R.A. Lebensohn, A.D. Rollett, P. Suquet, ~~Fast fourier transform-based modeling for the determination of micromechanical fields in polycrystals~~, JOM 63 (2011) 13–18.

## Tables

Table 1 A literature survey of CRSS values and ratios with respect to prismatic slip (in parentheses) of different slip and twin modes in pure Ti. The oxygen concentration and average grain size from each reference are also shown if they are reported.

prismatic	basal	pyr <a>	pyr <c+a>	T1 twin	O (wt%)	Grain size (μm)	Ref.
N/A	N/A	N/A	N/A (<13)	N/A	0.10	50	[6]
N/A	N/A (3.6)	N/A (25.4)	N/A (22.5)	N/A	0.25	115	[7]
120MPa	182MPa (1.5)	149MPa (1.2)	240MPa (2.0)	N/A	0.16	40	[8]
37MPa	49MPa (1.3)	N/A	197MPa (5.3)	213MPa (5.8)	<0.01	N/A	[10]
30MPa	150MPa (5.0)	N/A	120MPa (4.0)	125MPa (4.2)	<0.01	30	[11]
60MPa	120MPa (2.0)	N/A	180MPa (3.0)	125MPa (2.1)	0.17	80	[12,13]
80MPa	90MPa (1.1)	110MPa (1.4)	260MPa (3.3)	220MPa (2.8)	0.06	25	[14]
98MPa	N/A	N/A	224MPa (2.3)	136MPa (1.4)	<0.001	20	[15]
68MPa	175MPa (2.6)	120MPa (1.8)	250MPa (3.7)	230MPa (3.4)	0.12	50	[16]
90MPa	180MPa (2.0)	140MPa (1.6)	210MPa (2.3)	N/A	0.11	9	[17]
181MPa	209MPa (1.2)	N/A	474MPa (2.6)	N/A	0.07	N/A	[18]*
110MPa	N/A	N/A	N/A	N/A	0.07	N/A	[19]**
96±18MPa	127±33MPa (1.7–2.1)	N/A	≥240MPa (≥2.4)	225MPa (2.3)	0.17	100	this work

\* without considering sample size effect

\*\* after considering sample size effect

Table 2 Chemical composition of the material under investigation (wt%)

Element	O	Fe	Al	Cu	C	Ni	S	Cr	N	Ti
Fraction	0.17	0.049	0.017	0.017	0.015	0.013	0.011	0.011	0.004	bal

1  
2  
3  
4  
5  
6 **Table 3. Average error bars for grain orientation ( $\Delta\theta$ ), COM position ( $\Delta X$ ,  $\Delta Y$ ), and elastic strain**  
7 **components ( $\Delta e_{XX}$ ,  $\Delta e_{ZZ}$ ,  $\Delta e_{XY}$ ) at three load steps. For comparison, average values of elastic**  
8 **strain components ( $e_{XX}$ ,  $e_{ZZ}$ ,  $e_{XY}$ ) at these load steps are also shown.**

		Average grain error bars						Average elastic strain		
Load step	Peaks per grain	$\Delta\theta$ (°)	$\Delta X$ (μm)	$\Delta Y$ (μm)	$\Delta e_{XX}$ ( $10^{-4}$ )	$\Delta e_{ZZ}$ ( $10^{-4}$ )	$\Delta e_{ZX}$ ( $10^{-4}$ )	$e_{XX}$ ( $10^{-4}$ )	$e_{ZZ}$ ( $10^{-4}$ )	$e_{ZX}$ ( $10^{-4}$ )
1 ( $\epsilon=0$ )	56	0.30	22	31	3.3	3.2	2.3	-3.8	-1.2	-0.2
9 ( $\epsilon=0.31\%$ )	54	0.31	23	32	3.4	3.2	2.3	-13	22	-2.5
29 ( $\epsilon=2.6\%$ )	50	0.44	28	37	3.9	3.7	2.7	-14	31	-3.0

## Figure Captions

Fig. 1. Far-field HEDM setup at APS 1-ID along with the coordinate system used for data analysis. The sample was deformed in tension with 30 incremental steps, followed by 7 steps of unloading, as shown in the stress-strain curve.

Fig. 2. (a) {0001} pole figure of the 104 indexed grains in layer 6 before deformation. (b) Grain COM map on the cross section plane. The 17 analyzed grains are marked based on the identified slip activity in each of them.

Fig. 3. Evolution of the disorientation, c-axis misalignment, and the von Mises stress in four grains that show prismatic slip activity. The initial orientation for each grain is represented by a hexagonal cell in [the X-Y plane](#) [these images, with the tensile axis pointing out of the page](#). Orientation difference between the last loading step and a step at earlier deformation (marked by [the two arrows](#)), expressed in a rotational angle  $\theta_{\text{rot}}$  convention, are also shown ( $\theta_{\text{rot}}$ ). The rotational axis is defined in the crystal orthogonal coordinate system ( $x_1, x_2, x_3$ ) illustrated in the hexagonal unit cell on the right.

Fig. 4. Evolution of  $\tau_{\text{prism}}$ ,  $\tau_{\text{basal}}$ , and  $\tau_{c+a}$  with strain in Grains 90, 95, 99, and 101. For each grain, instantaneous von Mises stress ( $\sigma_{\text{VM}}$ ),  $\tau_{\text{prism}}$ ,  $\tau_{\text{basal}}$ , and  $\tau_{c+a}$  when prismatic slip was activated are shown.

Fig. 5. Distribution of the CRSS value for prismatic slip identified in 18 grains and basal slip identified in 22 grains.

Fig. 6. Evolution of the disorientation, c-axis misalignment, and the von Mises stress in four grains that show predominant basal slip activity. The increase in c-axis misalignment was almost equal to the increase of disorientation throughout the loading. This suggests that the grain rotation was mainly achieved by gradually tilting the c-axis, as illustrated for the specific

example of activation of one basal slip resulting in rotation about  $<10\bar{1}0>$  rotation axis. The disorientation between the last loading step and a step at early deformation (marked by the two arrows) are also shown ( $\theta_{\text{rot}}$ ).

Fig. 7. Evolution of  $\tau_{\text{prism}}$ ,  $\tau_{\text{basal}}$ , and  $\tau_{<\text{c+a}>}$  with strain in Grains 2, 5, 29, and 69. For each grain, instantaneous von Mises stress ( $\sigma_{\text{VM}}$ ),  $\tau_{\text{prism}}$ ,  $\tau_{\text{basal}}$ , and  $\tau_{<\text{c+a}>}$  when basal slip was activated are shown.

Fig. 8. Evolution of the disorientation, c-axis misalignment, and the von Mises stress for Grains 4, 36, 47, 12, 14, 91, 60, 61, and 65. The initial orientation of each grain is represented by a hexagonal cell in the X-Y plane these images, with the tensile axis pointing out of the page.

Fig. 9. Evolution of  $\tau_{\text{prism}}$ ,  $\tau_{\text{basal}}$ , and  $\tau_{<\text{c+a}>}$  with strain in Grains 4, 36, 47, 12, 14, 91, 60, 61, and 65.

Fig. 10. Von Mises stress ( $\sigma_{\text{VM}}$ ) in different grains in layer 6 when the macroscopic strain was (a) at 0, (b) at 0.31%, and (c) at 2.6%. The values of  $\sigma_{\text{VM}}$  (in MPa) are shown next to the COM of each grain, and the COM is colored according to this value. (d) Comparison of the average von Mises stress among all grains in layer 6 with the macroscopic tensile stress applied on the sample.

Fig. 1011. (a) Reconstructed grain map from the top slice of the near-field HEDM scan. Each grain is colored according to the angle between its c-axis and the Z direction: toward red if that angle is close to 0; toward blue if that angle is close to 90°. (b) {0001} pole figure generated from the grain orientations. Grains 1, 2, 4, 5, 12, 14, 47, 61, 65, 69, 90, 91, 95, and 101 are marked in both the grain map and the pole figure.

1  
2  
3  
4 Fig. 4412. Instantaneous  $\tau_{\text{prism}}$  and  $\tau_{\text{basal}}$  for the 18 grains that show prismatic slip (red circle) and  
5 22 grains that show basal slip (blue square). Grains with a free surface are also distinguished  
6 from grains from the interior volume. From that, the CRSS ratio between basal slip and  
7 prismatic slip is estimated to be between 1.7 and 2.1.  
8  
9

10  
11  
12  
13  
14 Fig. 4213. Effect of grain size and free surface on the CRSS for (a) the 18 grains that show  
15 prismatic slip and (b) the 22 grains that show basal slip.  
16  
17  
18  
19  
20  
21  
22  
23  
24  
25  
26  
27  
28  
29  
30  
31  
32  
33  
34  
35  
36  
37  
38  
39  
40  
41  
42  
43  
44  
45  
46  
47  
48  
49  
50  
51  
52  
53  
54  
55  
56  
57  
58  
59  
60  
61  
62  
63  
64  
65

**Figure 1**

[Click here to download high resolution image](#)

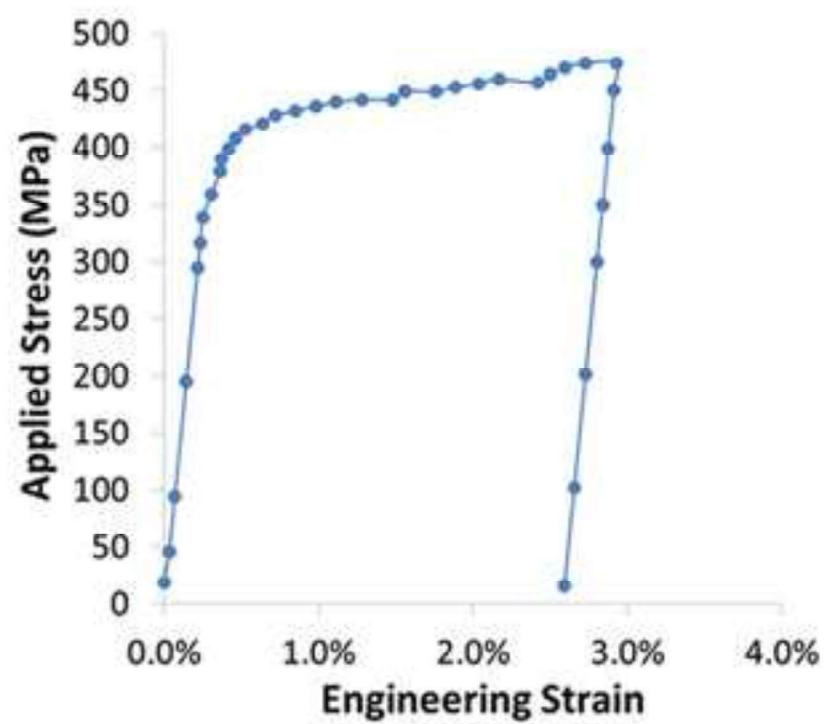
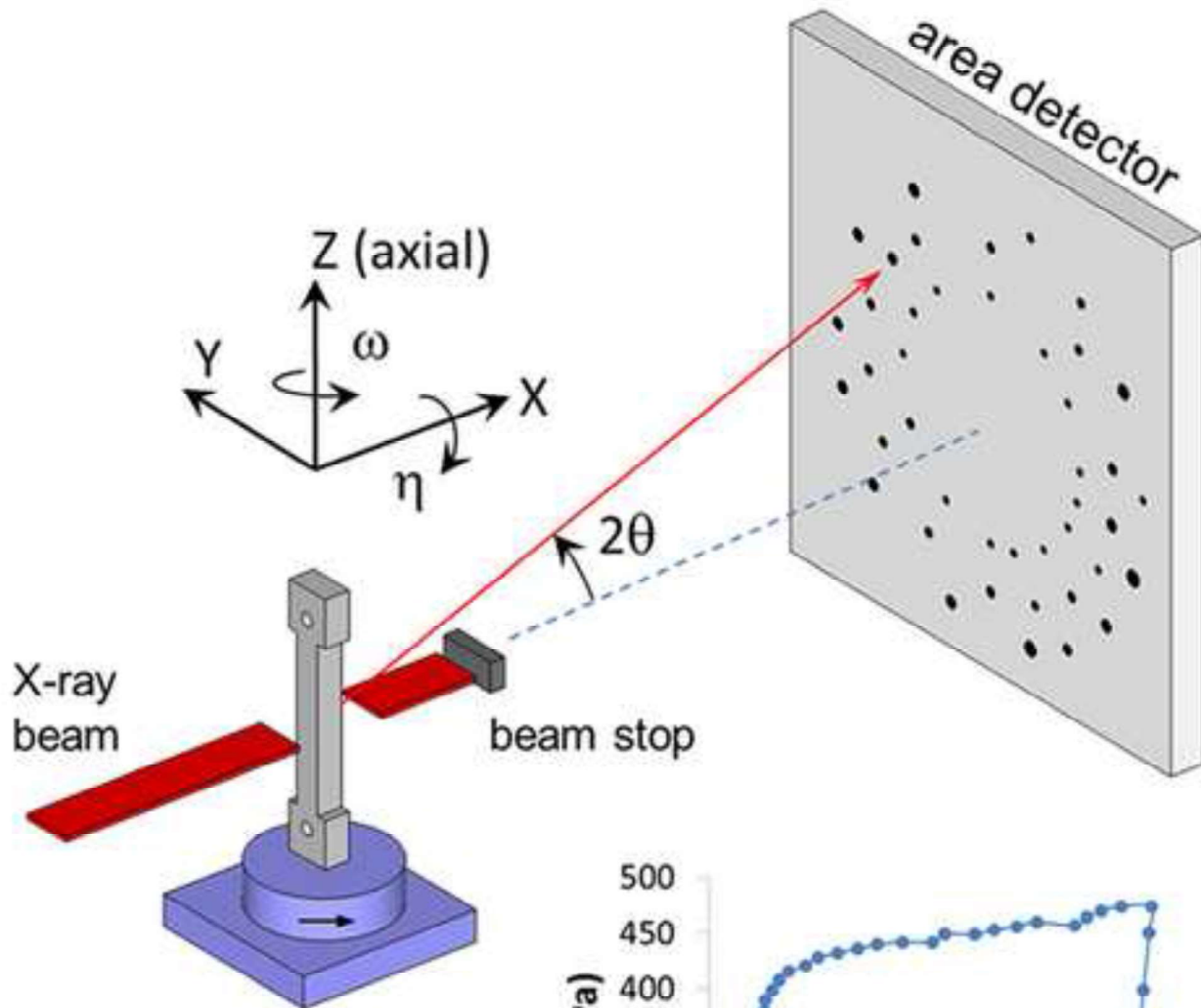
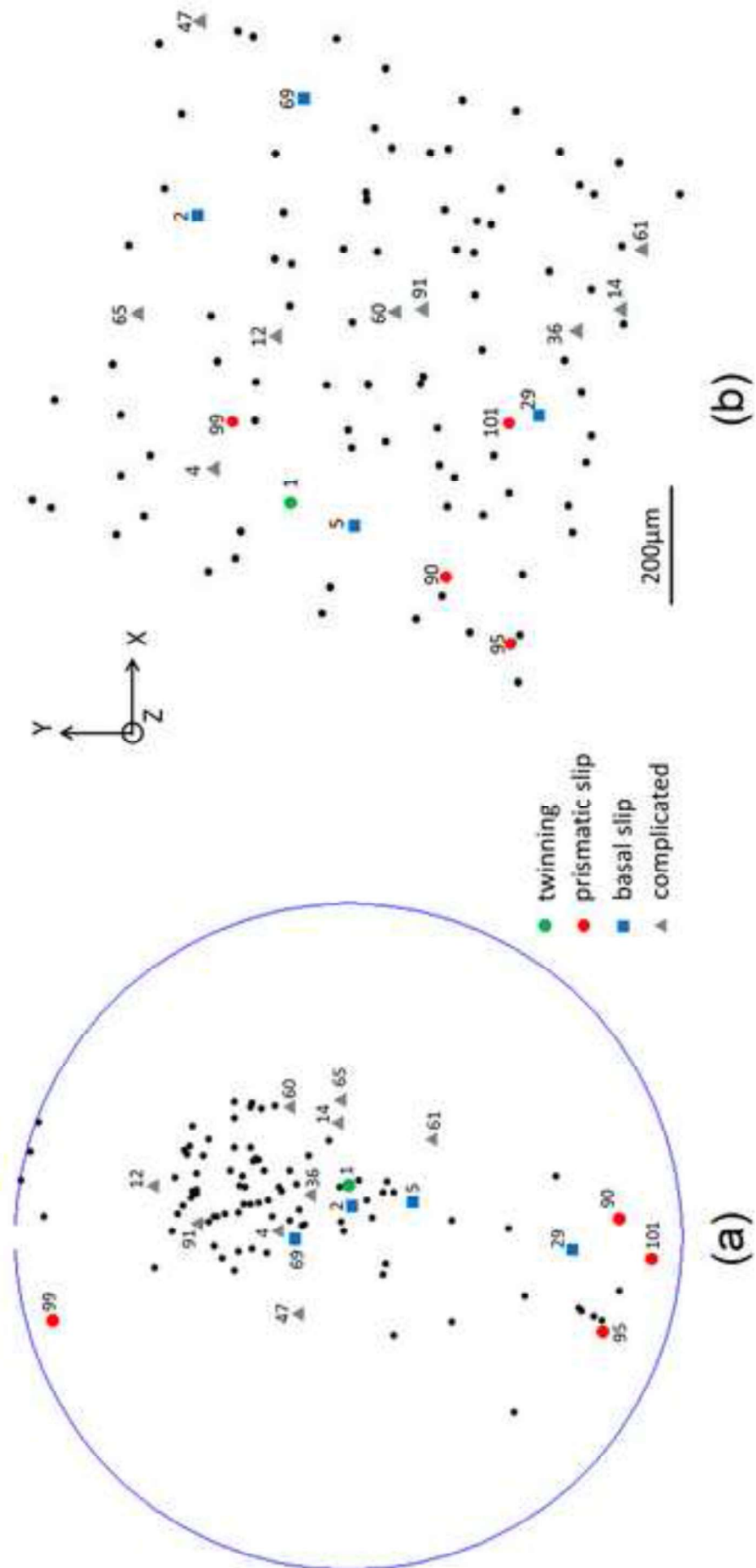


Figure 2 (revised)  
[Click here to download high resolution image](#)



**Figure 3**  
[Click here to download high resolution image](#)

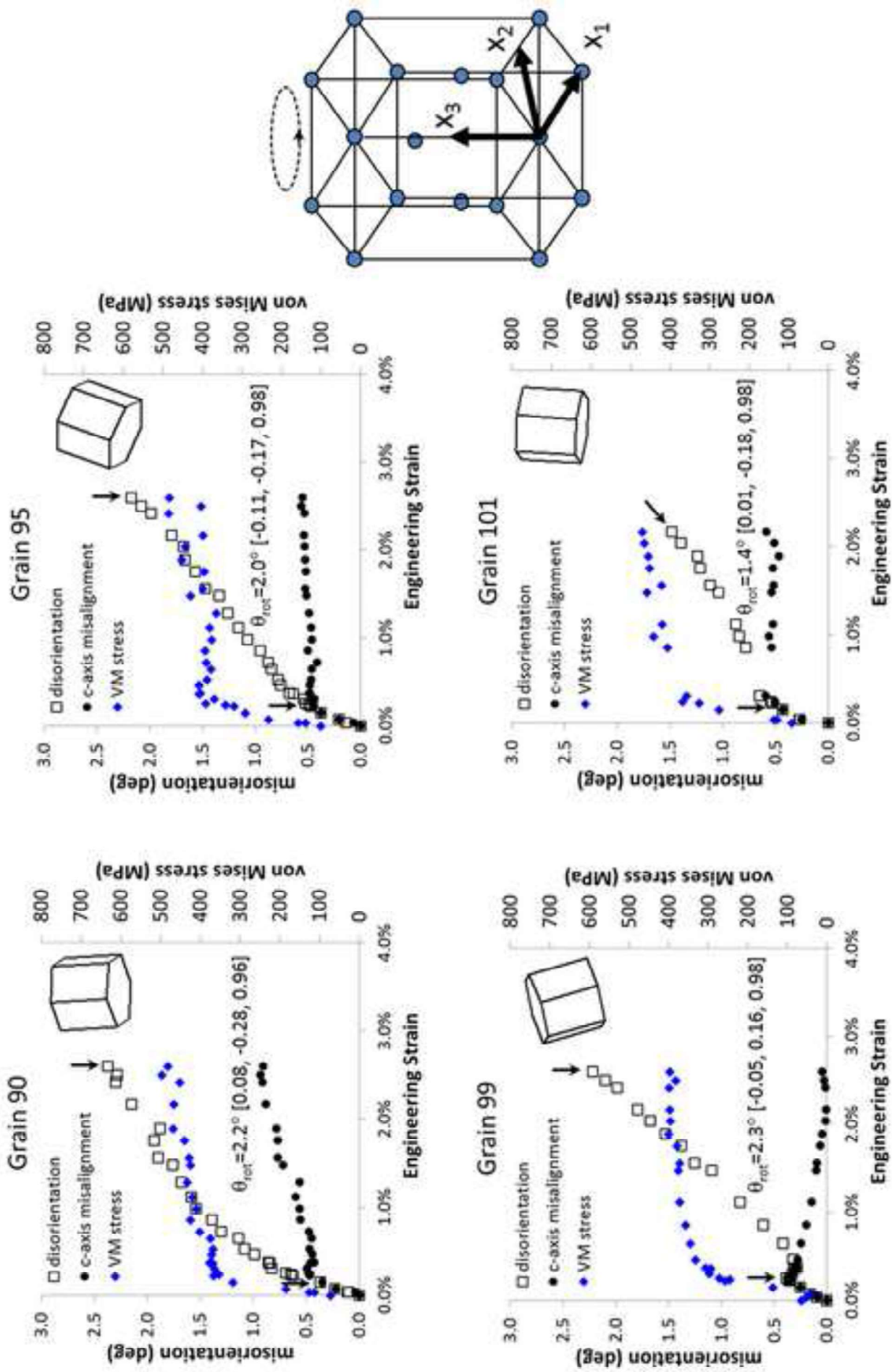
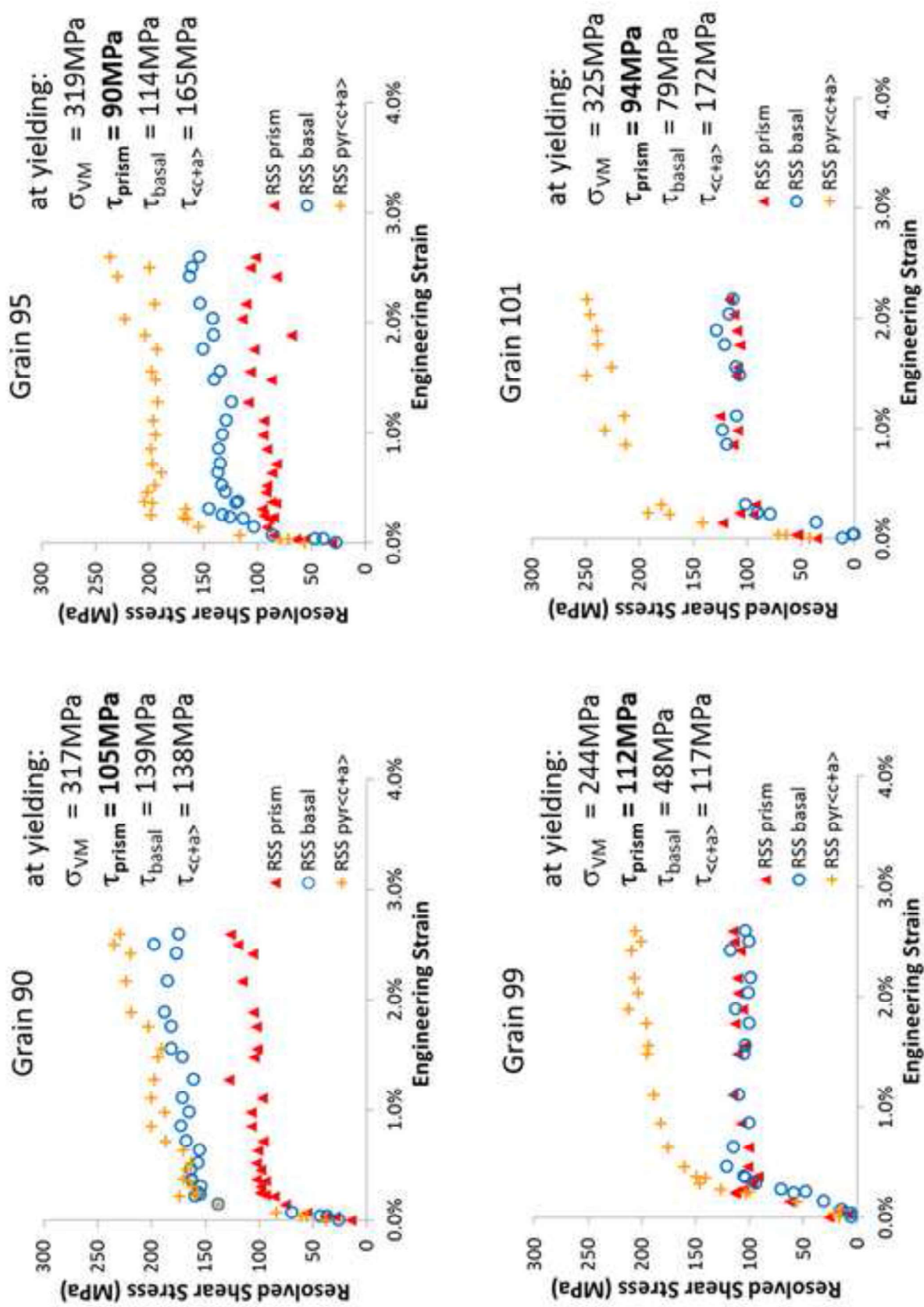


Figure 4 (revised)  
[Click here to download high resolution image](#)



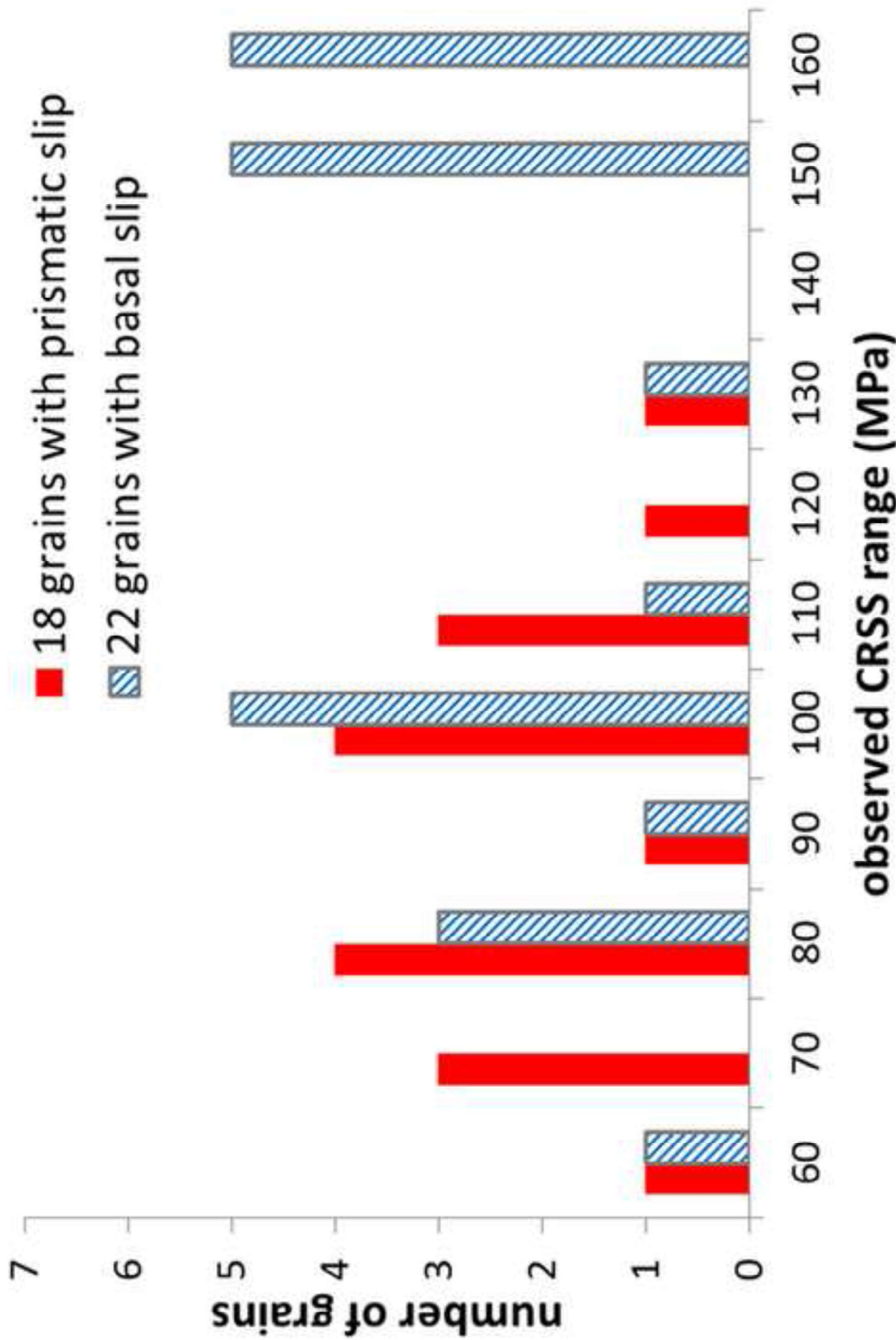


Figure 5 (revised)  
Click here to download high resolution image

**Figure 6**  
[Click here to download high resolution image](#)

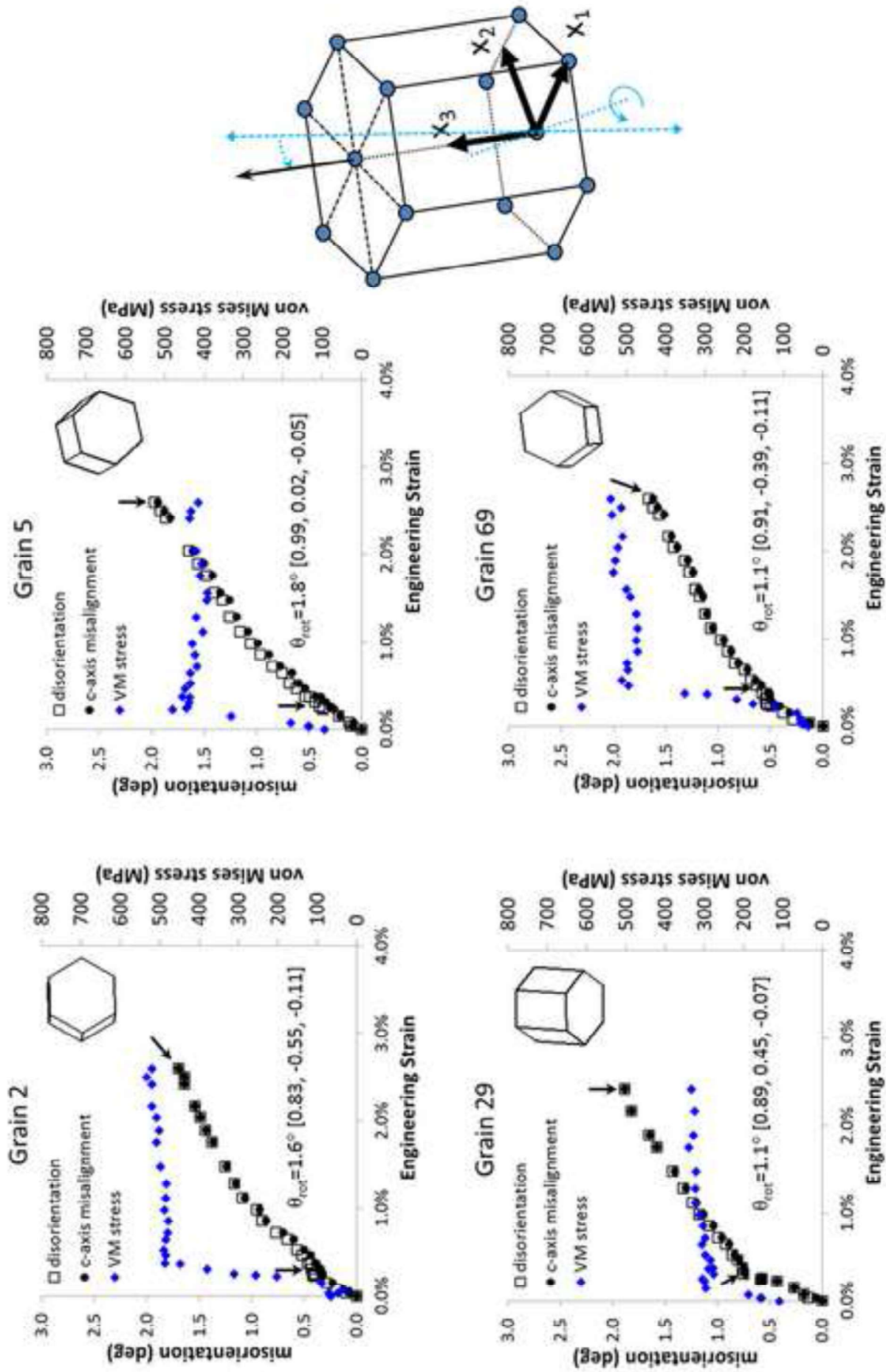
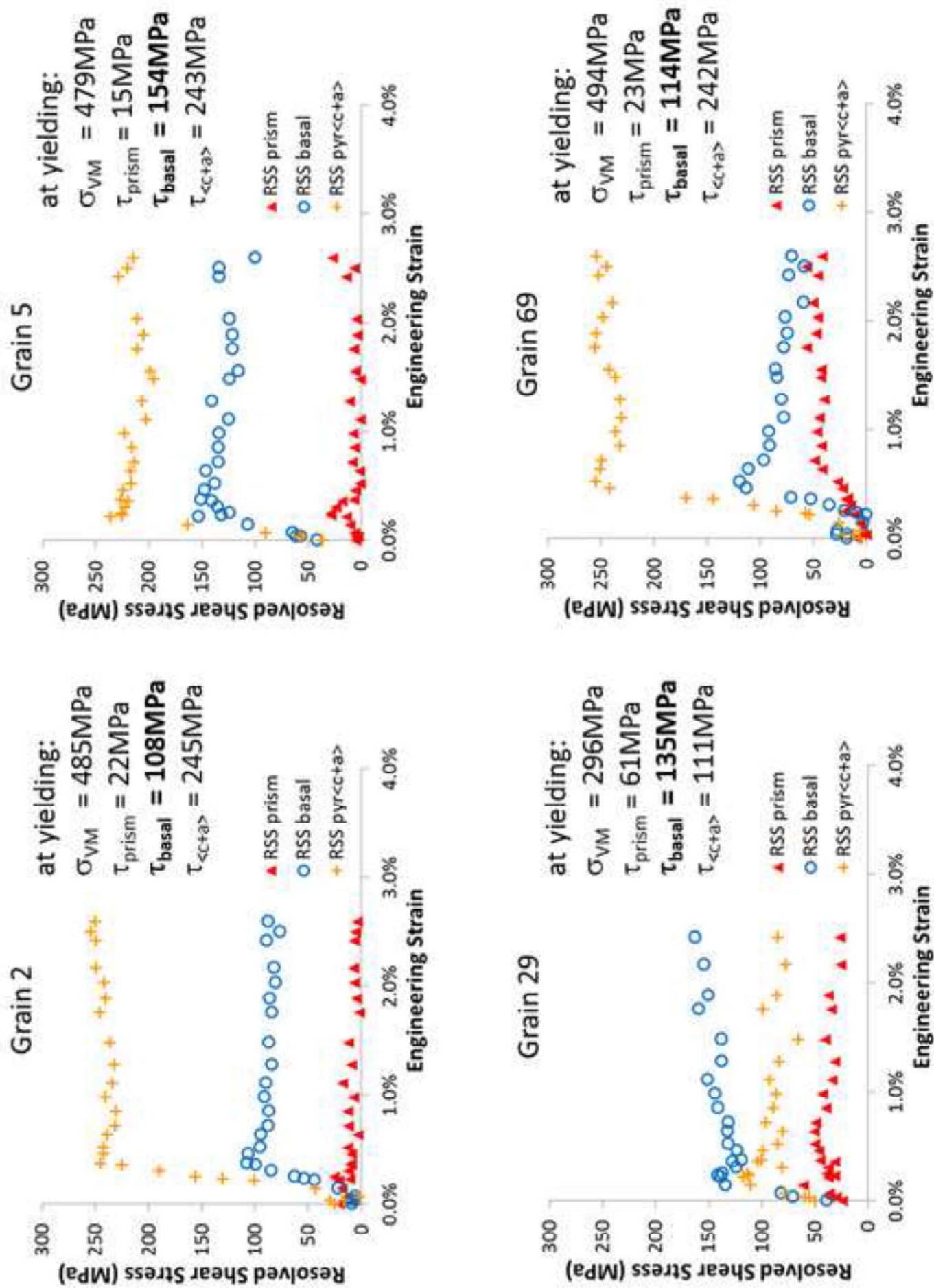
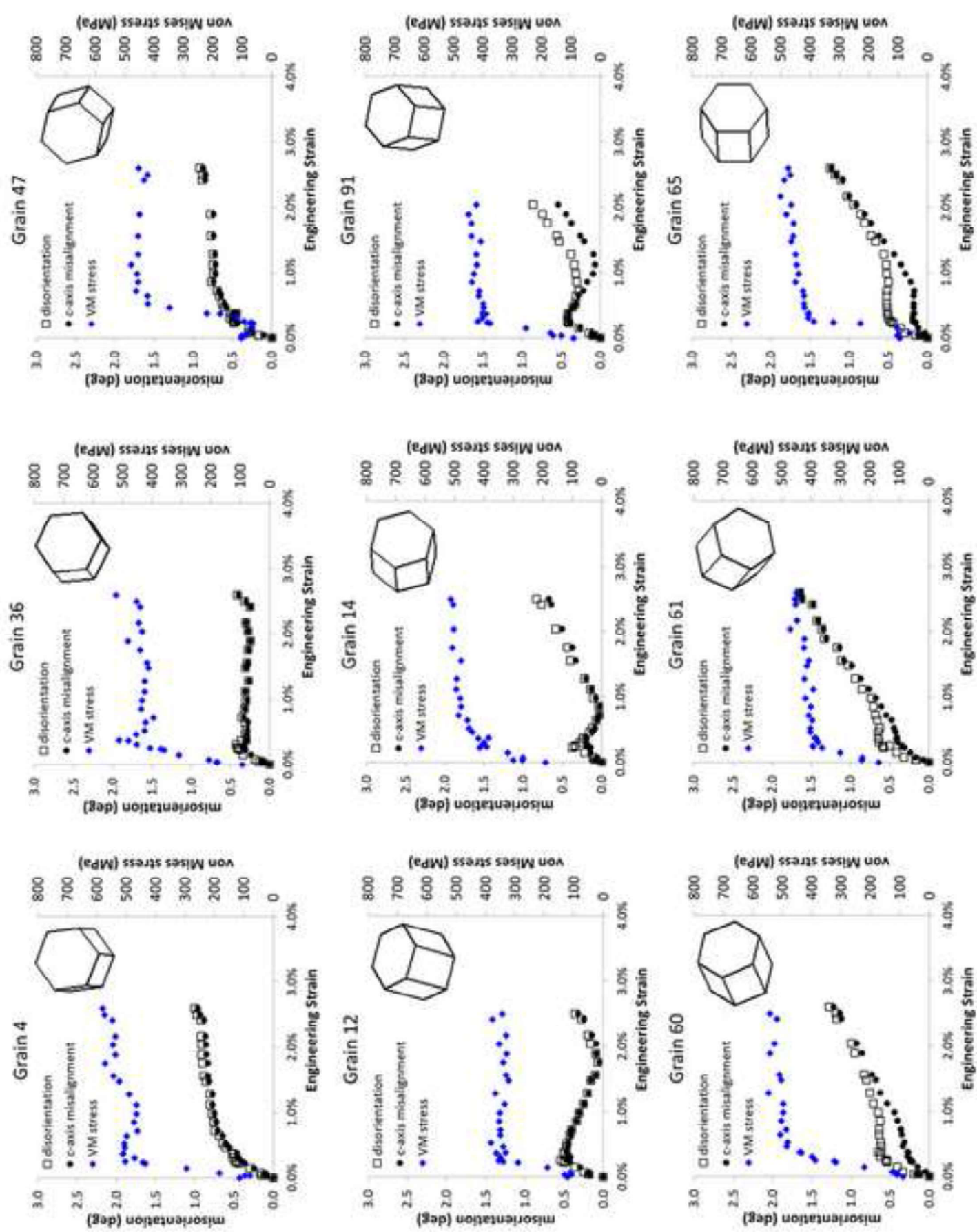


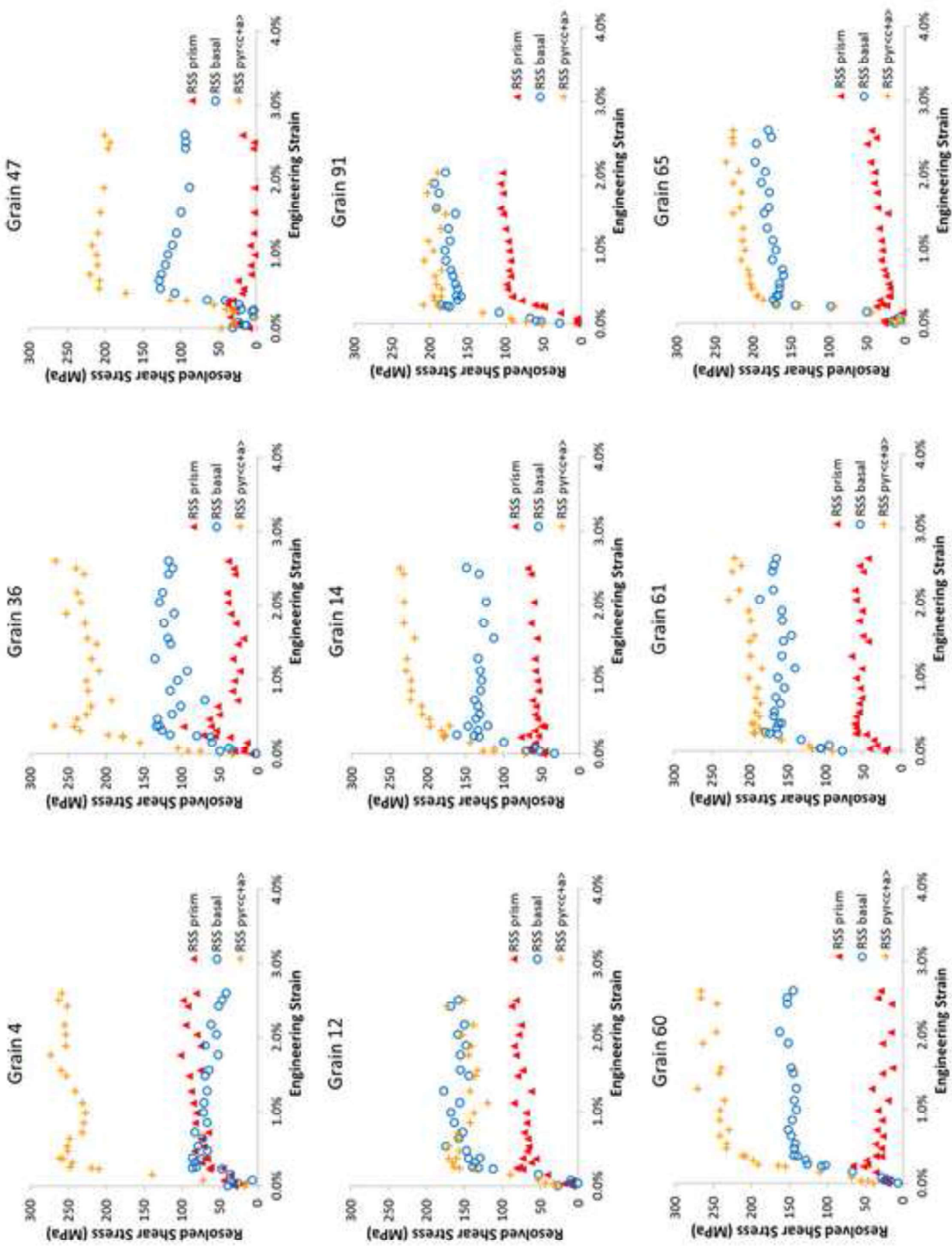
Figure 7 (revised)  
[Click here to download high resolution image](#)



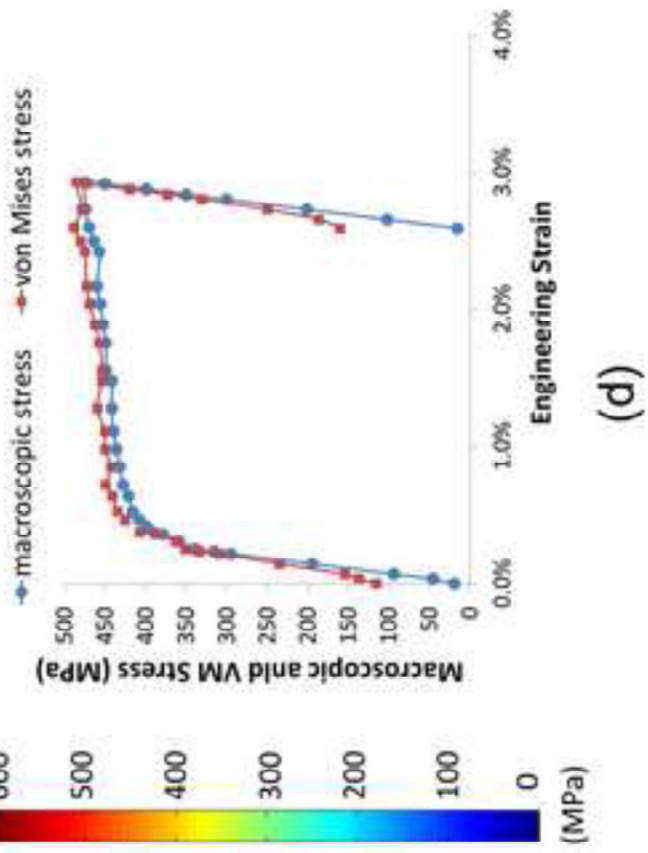
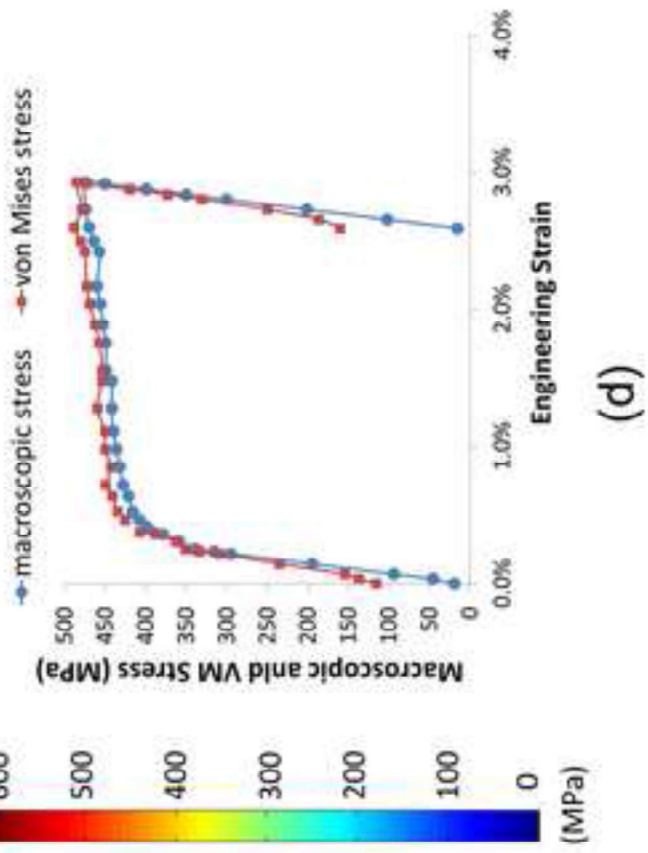
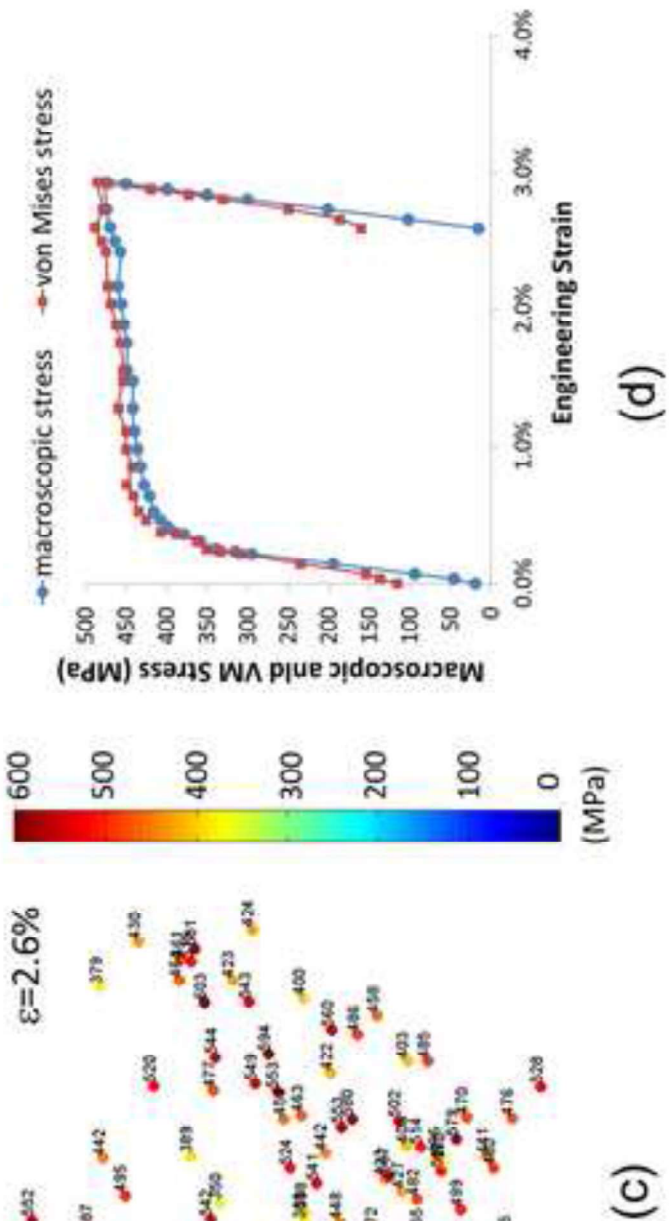
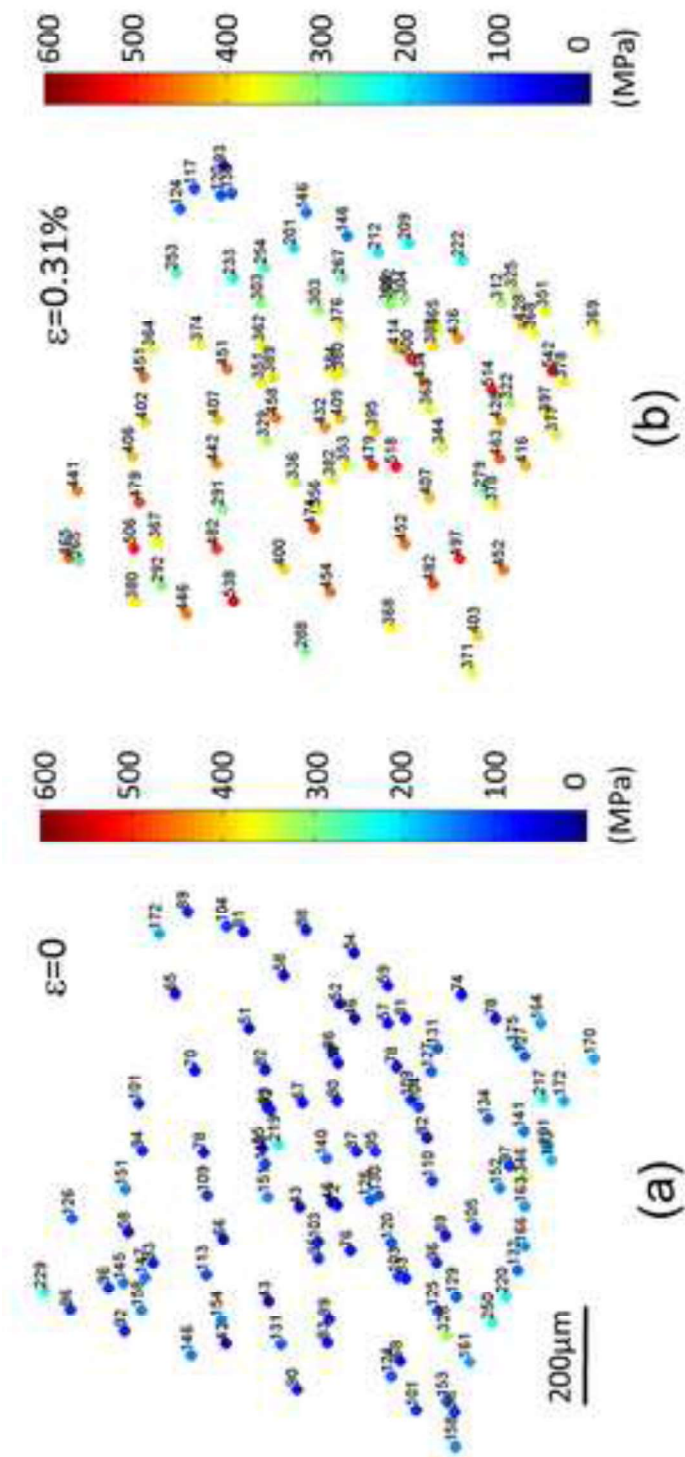
**Figure 8**  
[Click here to download high resolution image](#)



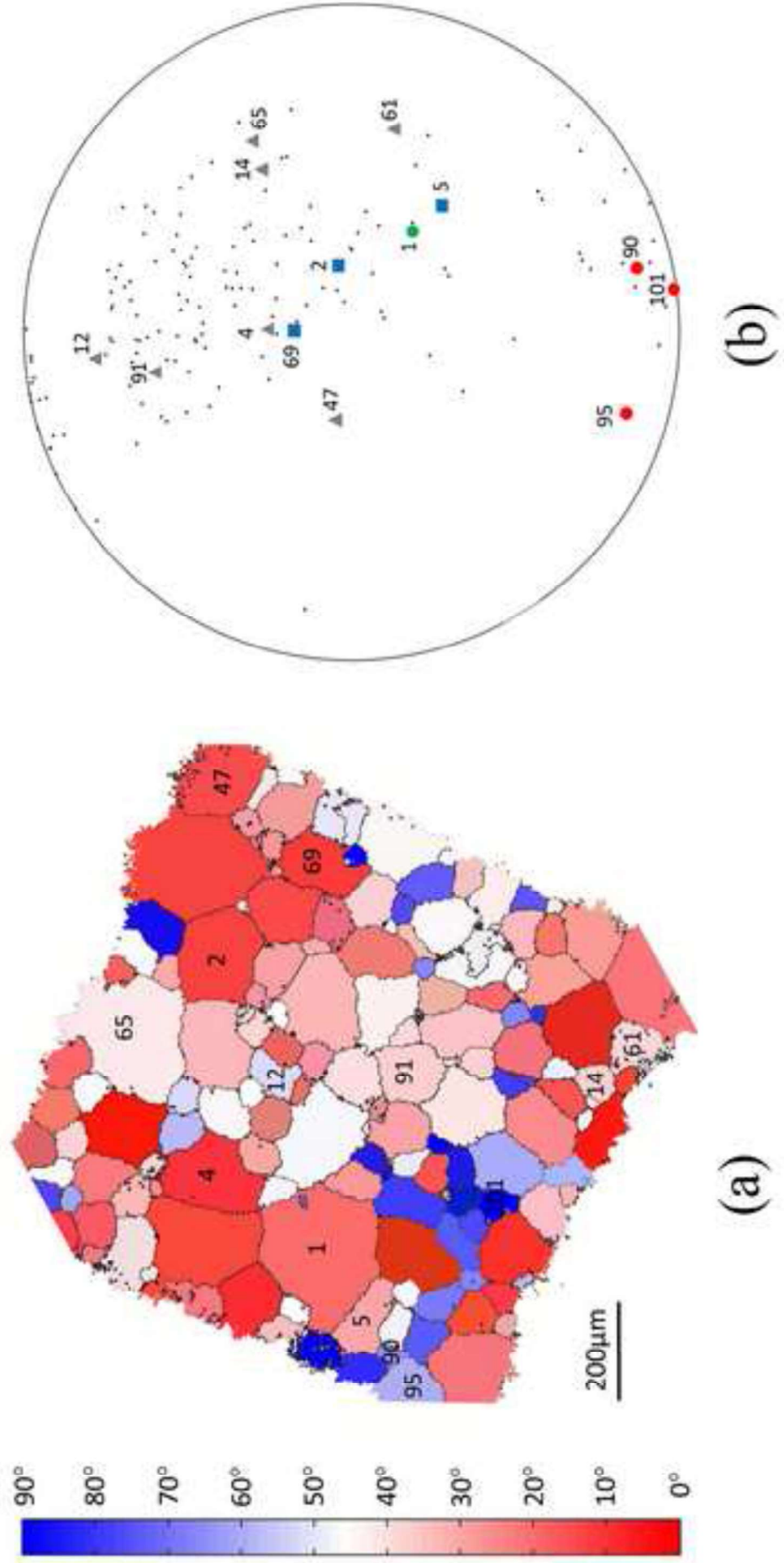
**Figure 9 (revised)**  
[Click here to download high resolution image](#)



**Figure 10 (revised)**  
[Click here to download high resolution image](#)



**Figure 11 (revised)**  
[Click here to download high resolution image](#)



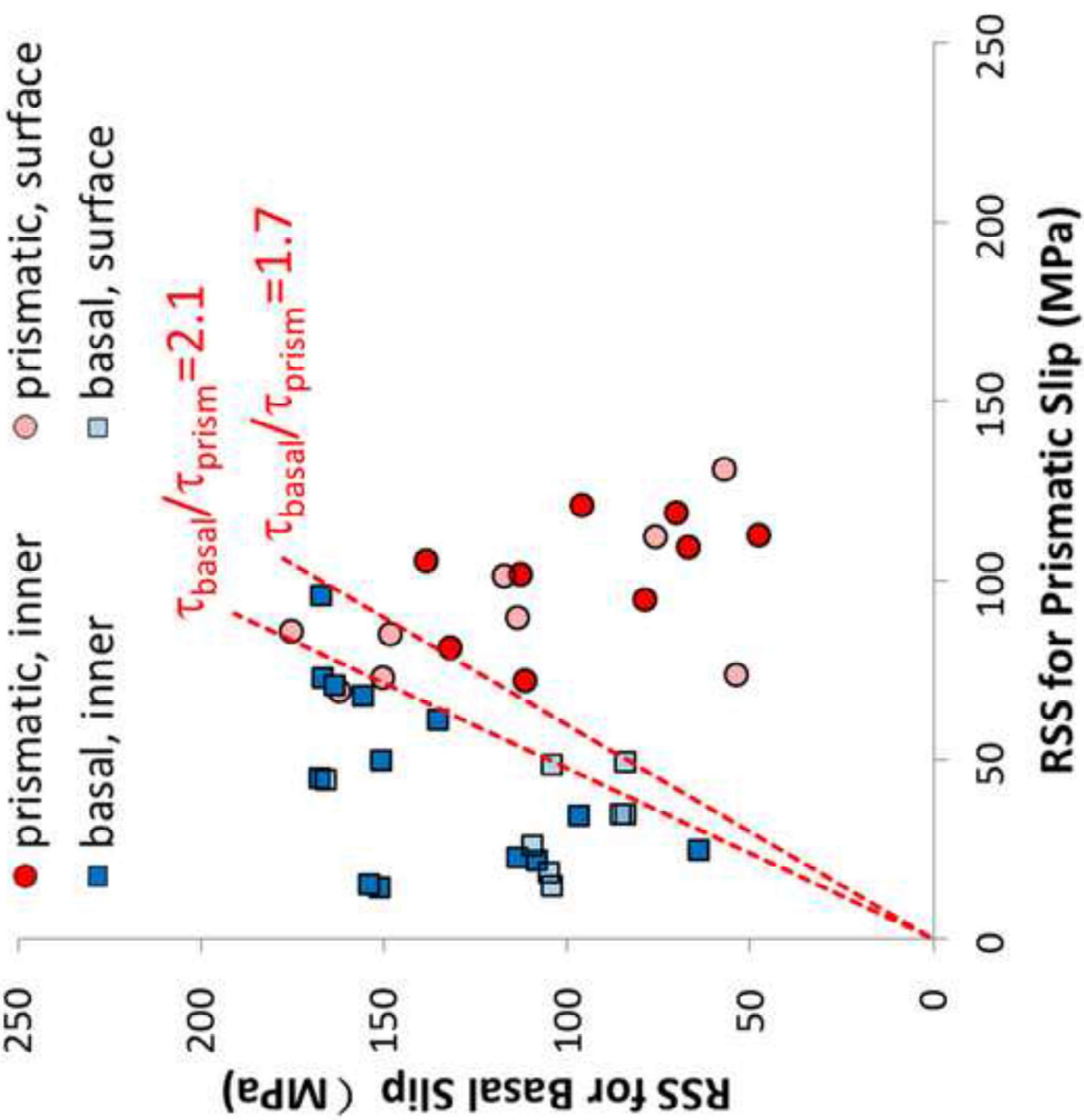
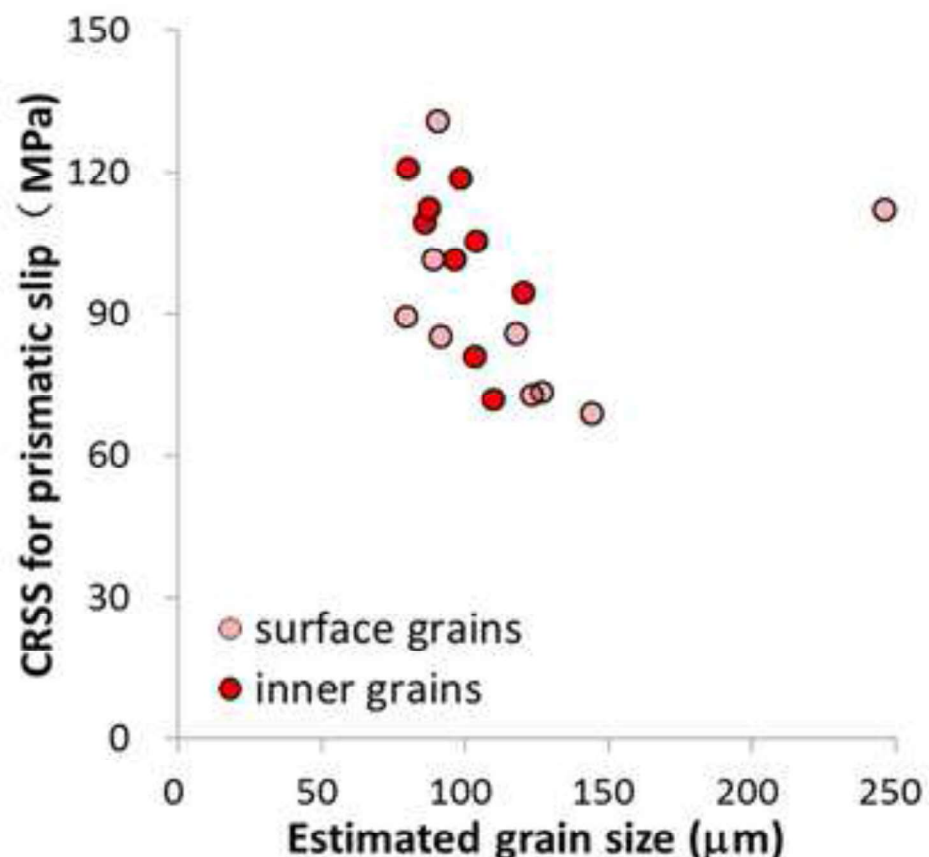
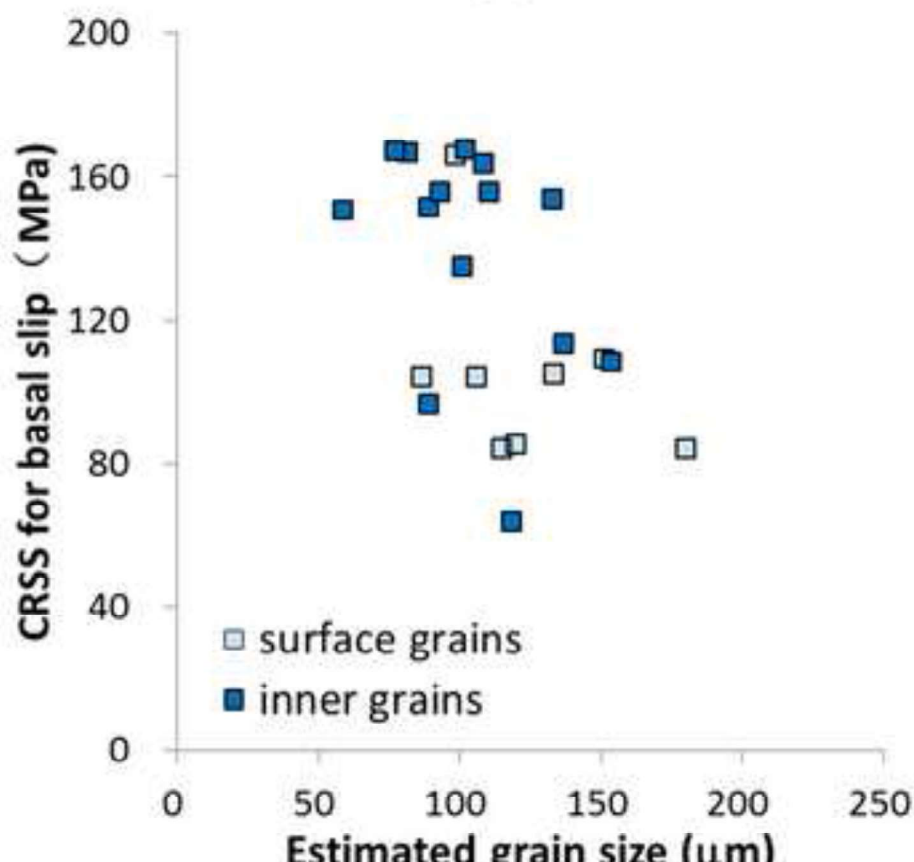


Figure 12 (revised)  
[Click here to download high resolution image](#)

Figure 13 (revised)

[Click here to download high resolution image](#)

(a)



(b)

